

Physics-Based Forecasting of Tomorrow’s Solar Wind at 1 AU

Igor V. Sokolov^{a,*}, and Tamas I. Gombosi^a

^aCenter for Space Environment Modeling, University of Michigan, 2455 Hayward St, Ann Arbor, MI, 48109, USA

Abstract

A faster than real time forecast system for solar wind and interplanetary magnetic field transients that is driven by hourly updated solar magnetograms is proposed to provide a continuous nowcast of the solar corona ($< 0.1\text{AU}$) and 24-hours forecast of the solar wind at 1 AU by solving a full 3-D MHD model. This new model has been inspired by the concept of *relativity of simultaneity* used in the theory of special relativity. It is based on time transformation between two coordinate systems: the solar rest frame and a boosted system in which the current observations of the solar magnetic field and tomorrow’s measurement of the solar wind at 1 AU are simultaneous. In this paper we derive the modified governing equations for both hydrodynamics (HD) and magnetohydrodynamics (MHD) and present a new numerical algorithm that only modifies the conserved quantities but preserves the original HD/MHD numerical flux. The proposed method enables an efficient numerical implementation, and thus a significantly longer forecast time than the traditional method.

Keywords: Solar wind, forecast, faster than real-time simulation, solar-terrestrial environment

1. Introduction

1.1. Mathematical Motivation

Yogi Berra, the legendary baseball player and philosopher, is credited with saying, “It’s tough to make predictions, especially about the future.” In modern times data assimilative physics-based models revolutionized short-term weather forecasts. These models combine physics models with real-time data from satellites, radar, and weather stations to provide detailed and reliable forecasts for up to three days. Unfortunately, we do not have similar advances in space weather forecasting due to the sparsity of data sources, the vast volume of space needed to be modeled for 24h to 72h forecasting, the lack of advanced data assimilation technologies incorporating sparse observations to model forecasts and the absence of high quality parameterizations of subgrid physical processes.

A new way to forecast solar wind is driven by the concept of “*relativity of simultaneity*.” For example, consider a “Lorentz boosted” or “boosted” frame of reference, moving with a relativistic velocity of Λ parallel to the x-axis in three-dimensional (3-D) Cartesian coordinates, $\mathbf{x} = (x, y, z)$ with respect to the rest frame. Herewith, and throughout this paper, the term “frame” combines the 4-D *spacetime* coordinates, $\mathbf{x}^{(4)} = (t, \mathbf{x})$ and the transformation between frames that includes the transformation of the time component, t .

*Corresponding author

Email addresses: igorsok@umich.edu (Igor V. Sokolov), tamas@umich.edu (and Tamas I. Gombosi)

Let us denote the spacetime coordinates in the boosted frame by subscript b , to distinguish them from those in the rest frame (no subscript). Now the transformation between the two systems, the *Lorentz boost*, is given by

$$\begin{aligned}
 t &= \Gamma \left(t_b + \frac{\Lambda}{c^2} x_b \right) \\
 x &= \Gamma \left(x_b + \Lambda t_b \right) \\
 y &= y_b \\
 z &= z_b
 \end{aligned} \tag{1}$$

where c is the limiting speed of the transformation (in special relativity this is the speed of light) and $\Gamma = 1/\sqrt{1 - \Lambda^2/c^2}$ is the Lorentz factor. Consider two events, which occurred simultaneously at time instant, $t_b^{(1)} = t_b^{(2)} = 0$, but at two different locations, $x_b^{(1)} = 0$ and $x_b^{(2)} > 0$. From the time transformation equations one can immediately see that in the rest frame the events are not simultaneous; they occur at time instants $t^{(1)} = 0$ and $t^{(2)} = (\Gamma\Lambda(x_b^{(2)} - x_b^{(1)}))/c^2$. The further apart the two locations are (increasing $\Delta x_b = x_b^{(2)} - x_b^{(1)}$), the further the rest frame time is ahead of the time t_b observed in the boosted frame. In Eq. (1) the speed of light represents the fastest speed allowed by Einstein’s special relativity: the spacetime transformation given by Eq. (1) can be mathematically defined as long as c is larger than the fastest speed in the system.

While this analogy is far from perfect, the idea of relativity of simultaneity inspired us to explore a new mathematical framework of a boosted frame, in which the time, t_b , coincides with the observation time of the latest solar magnetogram as well as with the measurement time of the “future” solar wind at 1 AU. Naturally, the time transformation is parameterized by some speed, which, similarly to the speed of light in Einstein’s special relativity, must exceed the maximum perturbation speed for mathematical validity of the approach.

1.2. Tomorrow’s Space Weather

The present generation of physics-based operational space weather models have limited prediction capabilities. The most widely used solar wind model, WSA-Enlil integrates an empirical model connecting solar magnetograms to solar wind speeds at around $20 R_\odot$ (Arge et al., 2011, 2013) and an 3-D MHD model of the inner heliosphere (Odstrčil, 2003; Odstrčil and Pizzo, 1999a,b). This model is used by NOAA’s Space Weather Forecast Office to provide a few days of advance warning of solar wind structures and Earth-directed coronal mass ejections (CMEs). While it is widely used, WSA-Enlil has several limitations, including simplistic inner boundary conditions for the interplanetary magnetic field and plasma density and the absence of magnetically driven CME initiation.

The operational SWMF/Geospace model (Tóth et al., 2005; Gombosi et al., 2021) is driven by *in situ* observations at the L1 point, and thus it only provides up to an hour forecast of the state of Earth’ magnetosphere. This forecast window is too short for practical use: by the time the warning of an upcoming geomagnetic storm is issued, the forecast has already expired. There is great need for a new space weather forecast system that starts at the Sun, provides a few days of forecast time at L1, and runs the Geospace model fast enough to provide at least a couple of days warning of upcoming geomagnetic storms.

This paper describes a “Sun2Mud” forecast model that can accomplish this objective. A new method for solving the governing equations of the solar wind and interplanetary magnetic field is proposed based on time shifting between the solar corona and inner heliosphere domains. These

domains already exist in the SWMF/AWSOM suite (Sokolov et al., 2013; van der Holst et al., 2014; Sokolov et al., 2021), and we only propose some modifications of the governing equations to allow a significant increase in the forecast time.

2. Time-shift Between the Corona and the Solar Wind

In the proposed model the 3-D MHD model of the coupled solar corona (SC) and inner heliosphere (IH) will run regularly to simulate the evolution during one hour of physical time. Every hour, we start a new simulation run from the previous final state, obtained with the last hourly magnetogram (taken an hour before) with this latest magnetogram as the time-dependent boundary condition at the solar surface. By the end of each simulation session, the solution in the SC is advanced until the time of next magnetogram. With reasonable computational resources, a computation time of less than one hour can be achieved, so that the recurrently simulated state in the SC lags only about an hour behind physical time.

Forecast capability is achieved with a special “boosted” frame in the IH computational domain ($R \geq R_{\text{SC/IH}}$, $R = \|\mathbf{x}\|$ is the heliocentric distance, $R_{\text{SC/IH}}$ is the radius of the boundary between SC and IH, where the two numerical models are coupled). This interface can be chosen to be at $R_{\text{SC/IH}} = 0.1$ AU where the solar wind is already super-Alfvénic. Below this interface the time in the boosted frame coincides with that in the rest frame:

$$t = t_b, \quad \mathbf{x} = \mathbf{x}_b, \quad R \leq R_{\text{SC/IH}} \quad (2)$$

At larger distances, $R > R_{\text{SC/IH}}$, the rest frame time exceeds the boosted frame¹ time by an R dependent offset:

$$t = t_b + \Delta t(R), \quad \Delta t(R) = \Delta t_0 \frac{R - R_{\text{SC/IH}}}{1 \text{ AU} - R_{\text{SC/IH}}}, \quad \mathbf{x} = \mathbf{x}_b, \quad (3)$$

where $\Delta t_0 = \Delta t(R = 1 \text{ AU})$ is the desired forecast interval at 1 AU. While the simulated time in the SC domain, t_{SC} , is about an hour behind the physical time, the time at 1 AU, $t_{\text{IH}}(R = 1 \text{ AU}) = t_{\text{SC}} + \Delta t_0$ is ahead of the physical time (for example, $\Delta t_0 = 25$ hours give about a day of forecast time, while $\Delta t_0 = 13$ h gives half a day forecast).

The offset time is a linear function of R , therefore the derivative $d[\Delta t(R)]/dR$ is constant. Its inverse characterizes the maximum “allowable CME speed,” Λ_m :

$$\frac{d(\Delta t)}{dR} = \frac{\Delta t_0}{1 \text{ AU} - R_{\text{SC/IH}}} = \frac{1}{\Lambda_m}. \quad (4)$$

For $\Delta t_0 = 25$ h we get $\Lambda_m = 1,500$ km/s, which means that the maximum radial speed of transients, $c_{R_{\text{max}}}$, allowed in the model cannot exceed this value. In fact, if a transient with radial speed, $c_{R_{\text{max}}} > \Lambda_m$ crosses the SC / IH boundary at the time instant $t = t_0$, it will reach 1 AU at $t_0 + (1 \text{ AU} - R_{\text{SC/IH}}) / c_{R_{\text{max}}} < t_0 + (1 \text{ AU} - R_{\text{SC/IH}}) / \Lambda_m = t_0 + \Delta t_0$. This time is *in the past* for

¹We note again that the analogy with the relativistic boost is far from perfect: although we took the idea of relativity of simultaneity from the first of Eqs.(1), in our case there is no relative motion of frames, since there is no time-dependent coordinate transformation, such as in the second of Eqs.(1).

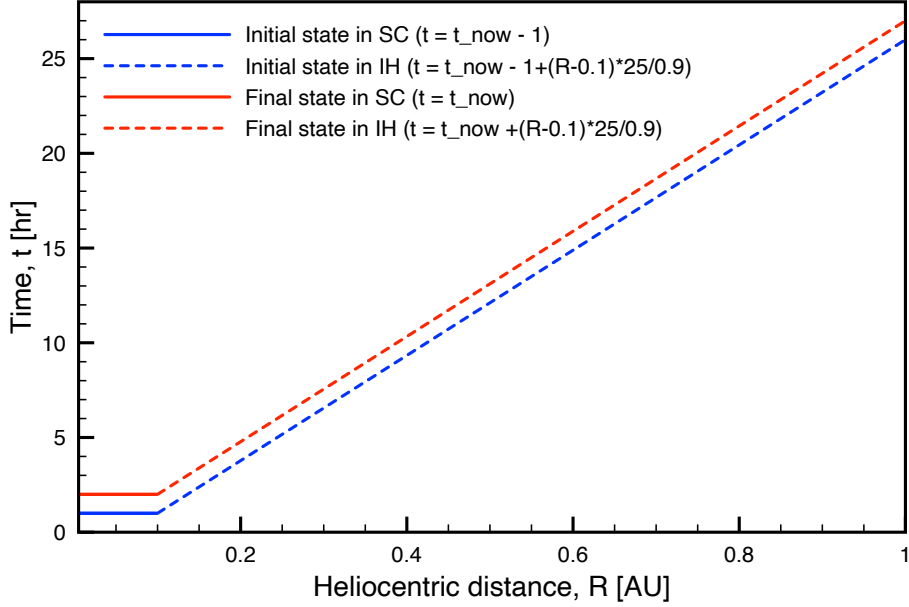


Figure 1: Space-time diagram for the proposed forecast model. The simulation time in SC corresponds to the physical time, the computational domain being $R_{\odot} \leq R \leq R_{\text{SC/IH}}$, $t_{\text{start}} \leq t_{\text{SC}} \leq t_{\text{final}}$. In the IH model, the computational domain with time offset is $R_{\text{SC/IH}} \leq R \leq 1 \text{ AU}$, $t_{\text{start}} + \Delta t(R) \leq t_{\text{IH}} \leq t_{\text{final}} + \Delta t(R)$. Herewith, $t_{\text{start}} = t_{\text{now}} - 1 \text{ h}$, $t_{\text{final}} = t_{\text{now}}$, t_{now} being the time of latest magnetogram.

which forecast is already available, thus violating causality. Since the speed of the fastest CMEs exceeds 1,500 km/s, one might use a better upper limit for the maximum allowable CME speed in order to avoid acausality, such as $\Lambda_m = 3,000 \text{ km/sec}$. Such a large value of Λ_m , however, would lower the applicable forecast time by a factor of 1/2. The restriction,

$$c_{R_{\text{max}}} < \Lambda_m, \quad (5)$$

which expresses the *causality principle* is one of the criteria for the applicability of the proposed governing equations and associated numerical methods.

It is relatively straightforward to apply/implement the proposed framework to a system of *conservation laws*, which is actually a set of partial differential equations (PDEs) of a special kind, mathematically expressing the conservation of physical quantities such as mass, momentum, and energy. Specifically, for each of these conserved quantities the *conservation laws* can be written as

$$\frac{\partial U}{\partial t} + \nabla \cdot \mathbf{F} = 0 \quad (6)$$

where U is the density of a *conserved variable* and $\nabla \cdot \mathbf{F}$ is the divergence of the flux function \mathbf{F} (at a given time).

In the SC computational domain the equations will be solved in a boosted frame with $\Delta t_0 = 0$ (rest frame) and they can be re-written in terms of $t_b = t$:

$$\frac{\partial U}{\partial t_b} + \nabla \cdot \mathbf{F} = 0, \quad R_{\odot} \leq R \leq R_{\text{SC/IH}}. \quad (7)$$

In the IH domain it is convenient to apply the coordinate transformation $(t, \mathbf{x}) \rightarrow (t_b, \mathbf{x})$ for Eq. (6). The spatial derivatives at constant t are converted to those at constant t_b the following way:

$$\begin{aligned} \frac{\partial}{\partial \mathbf{x}} (\dots)_{t=\text{const}} &= \frac{\partial}{\partial \mathbf{x}} (\dots)_{t_b=\text{const}} + \left(\frac{\partial t_b}{\partial \mathbf{x}} \right)_{t=\text{const}} \frac{\partial}{\partial t_b} (\dots)_{\mathbf{x}=\text{const}}, \\ \left(\frac{\partial t_b}{\partial \mathbf{x}} \right)_{t=\text{const}} &= \left(\frac{\partial (t - \Delta t)}{\partial \mathbf{x}} \right)_{t=\text{const}} = -\nabla(\Delta t) = -\frac{\hat{\mathbf{e}}_R}{\Lambda_m} \end{aligned} \quad (8)$$

$\hat{\mathbf{e}}_R$ being a unit vector in the radial direction. With the use of Eq. (8) the governing equations in IH can be written as follows:

$$\frac{\partial}{\partial t_b} \left(U - \frac{1}{\Lambda_m} \hat{\mathbf{e}}_R \cdot \mathbf{F} \right) + \nabla \cdot \mathbf{F} = 0, \quad R_{\text{SC/IH}} \leq R \leq 1 \text{ AU}. \quad (9)$$

We note that while the state variable is modified in Eq. (9), the flux function remains the same. This fact will greatly simplify the resulting predicting algorithm.

3. Proof of Concept Example

In order to illustrate the concept described in Sec. 2 we consider a 1-D continuity equation and compare its solutions in a rest frame and in a boosted frame for a solar wind moving in the x direction with a constant speed, u_0 that satisfies the $0 < u_0 < \Lambda_m$ condition (Λ_m is the limiting speed for the forecast). In our case the only relevant state variable is $U = \rho$ and the only relevant flux function is $F = \rho u_0$. In the rest frame Eq. (6) with these choices for U and F reads:

$$\frac{\partial \rho}{\partial t} + u_0 \frac{\partial \rho}{\partial x} = 0. \quad (10)$$

However, in the boosted frame Eqs. (7 and 9) (the latter is divided by $(1 - u_0/\Lambda_m)$) become

$$\frac{\partial \rho}{\partial t_b} + u_0 \frac{\partial \rho}{\partial x} = 0 \quad \text{if } R_{\odot} \leq x \leq R_{\text{SC/IH}} \quad (11)$$

$$\frac{\partial \rho}{\partial t_b} + u'_0 \frac{\partial \rho}{\partial x} = 0 \quad \text{if } R_{\text{SC/IH}} \leq x \leq 1 \text{ AU} \quad (12)$$

where $u'_0 = u_0/(1 - u_0/\Lambda_m)$. We note that $u'_0 > u_0$, because $0 < u_0/\Lambda_m < 1$. Therefore, any perturbation propagates faster in the boosted system than in the rest frame. This is the essence of the new forecast capability proposed in this paper.

Let us consider a specific example. Let $u_0 = 400$ km/s (typical slow solar wind speed) and $\Lambda_m = 800$ km/s. Let us chose 0.1AU for the SC-IH boundary and place the outer boundary at 1AU. In this case the length of the IH region is 0.9AU and the corresponding value of $\Delta t_0 = 0.95 \text{ AU}/\Lambda_m$ is $= 1.95$ days at 1AU (see Eq. 3). The initial condition is a uniform and constant density everywhere: $\rho(x) = 1$ at $t = t_b = 0$. At $t = 0$ we double the density at the SC-IH interface and keep it constant at later times. Therefore, in the rest frame the solution of Eq. (10) is: $\rho = 2$ at $x - R_{\text{SC/IH}} < u_0 t$ and $\rho = 1$ at $x - R_{\text{SC/IH}} > u_0 t$. However, in the boosted frame, the solution becomes: $\rho = 2$ at $x - R_{\text{SC/IH}} < u'_0 t_b$ and $\rho = 1$ at $x - R_{\text{SC/IH}} > u'_0 t_b$. Fig. 2 shows the results at the orbits of the terrestrial planets. One can see that the forecast time at Mercury is less than a day,

at Venus it is a day and a half, while at Earth the forecast time is about two days. This forecast time inversely depends on the limiting speed, Λ_m . If we chose a reasonable value that exceeds most CME speeds (like $\Lambda_m = 1,500\text{km/s}$) the forecast time ($\Delta t_0 = 0.9\text{AU}/\lambda_m$) decreases to about a day. With an upper limit for space-age CMEs ($\Lambda_m = 3,000\text{km/s}$) we still get a 12h forecast time.

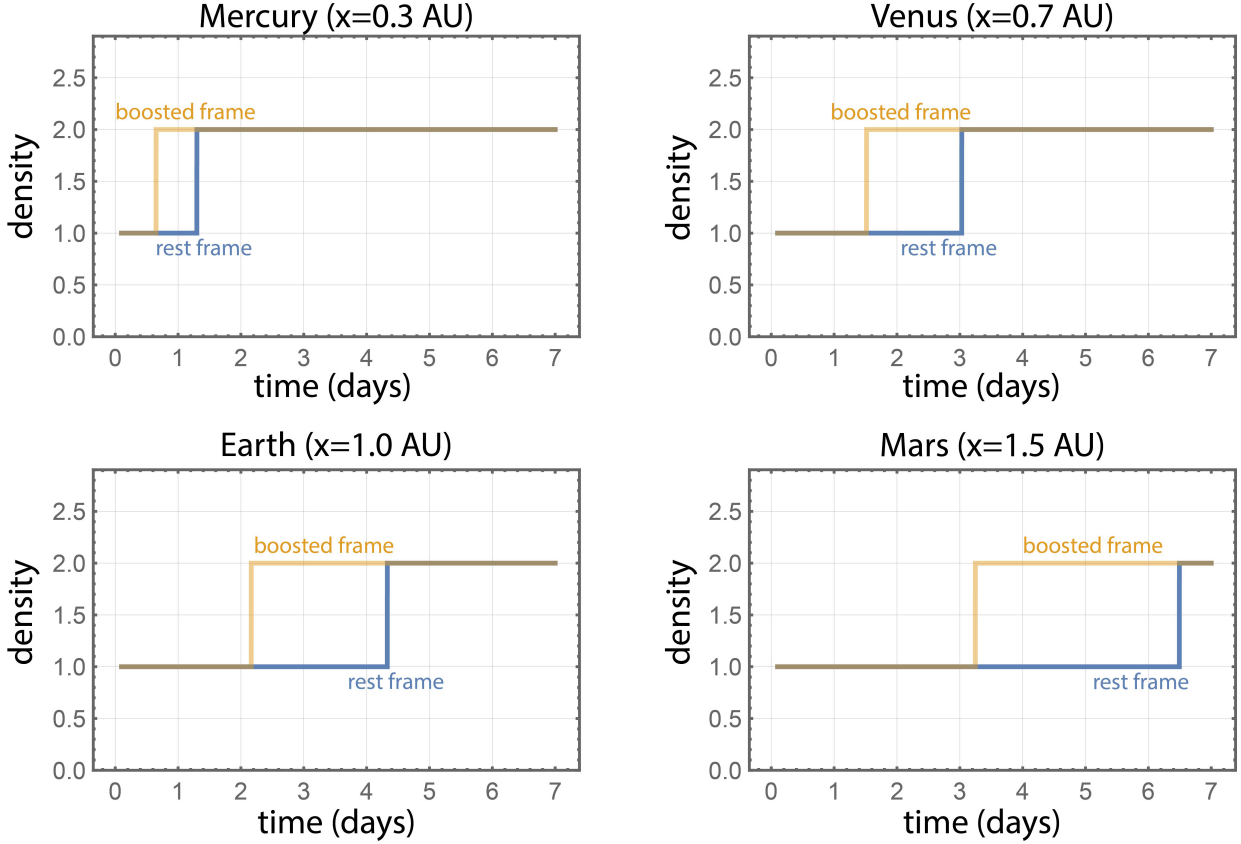


Figure 2: Time evolution of the density at several radial distances following a sudden density increase at $x = 0.1$ AU at $t = 0$.

4. Characteristic Properties of the Modified Governing Equations

4.1. Eigensystem

Although the system of conservation laws given by Eq. (6) is non-linear in the important cases of hydrodynamics (Landau and Lifshitz, 1959) or magnetohydrodynamics (MHD) (Shore, 1992), its properties are essentially characterized by the linearized *characteristic equations* for small perturbations. For waves propagating in the radial direction, the characteristic form of Eqs. (6) reads

$$\frac{\partial U_i}{\partial t} + \sum_j \frac{\partial (\hat{\mathbf{e}}_R \cdot \mathbf{F}_i)}{\partial U_j} \cdot \frac{\partial U_j}{\partial R} = 0, \quad (13)$$

where the conserved variables and their flux vectors are denoted with the subscript index i . If the system of conservation laws is *hyperbolic*, the Jacobian matrix, $\partial (\hat{\mathbf{e}}_R \cdot \mathbf{F}_i) / \partial U_j$, possesses a

full set of eigenvalues, $\lambda^{(\ell)}$, and corresponding eigenvectors. Each of the eigenvectors describes some linear combinations of (small increments in) conserved variables, which are referred to as *the Riemann invariants*, $\mathcal{R}^{(\ell)}$ and obey a set of independent linear advection equations:

$$\frac{\partial \mathcal{R}^{(\ell)}}{\partial t} + \lambda^{(\ell)} \frac{\partial \mathcal{R}^{(\ell)}}{\partial R} = 0, \quad (14)$$

in which the Jacobian eigenvalue plays the role of *characteristic speed*. The solution of this kind of equations is any function, $\mathcal{R}(R/\lambda^{(\ell)} - t)$ of a single argument, $(R/\lambda^{(\ell)} - t)$, which describes the wave propagation along the spacetime line, obeying the equation:

$$\frac{dt}{1} = \frac{dR}{\lambda^{(\ell)}}. \quad (15)$$

The denominators in Eq. (15) are equal to the factors multiplying the time and coordinate derivatives in Eq. (14).

While the above considerations are directly applicable to the SC domain, for the modified system of conservation laws used in the IH domain the characteristic equation (Eq. (9)) needs to be modified:

$$\left(1 - \frac{\lambda^{(\ell)}}{\Lambda_m}\right) \frac{\partial \mathcal{R}^{(\ell)}}{\partial t_b} + \lambda^{(\ell)} \frac{\partial \mathcal{R}^{(\ell)}}{\partial R} = 0, \quad (16)$$

which results in the modified equation for the characteristic spacetime line

$$\frac{dt_b}{1 - \frac{\lambda^{(\ell)}}{\Lambda_m}} = \frac{dR}{\lambda^{(\ell)}}, \quad (17)$$

corresponding to the modified characteristic speed of $\lambda^{(\ell)}/(1 - \lambda^{(\ell)}/\Lambda_m)$. For waves propagating outward from the Sun, i.e., for $\lambda^{(\ell)} > 0$, the waves propagate faster in the boosted frame than real time, thus providing the mathematical foundation for forecasting their arrival to 1 AU. Eq. (17) yet again demonstrates the necessity for the limiting speed, Λ_m given by Eq. (5), since if any eigenvalue, $\lambda^{(\ell)}$, would exceed Λ_m , the corresponding wave would propagate back in time (see Eq. 17). We also note that the characteristic speed in physical time does not change. Indeed, by substituting $dt_b = dt - d\Delta t = dt_{\text{IH}} - dR/\Lambda_m$ into Eq. (17) we get $dt = dR/\Lambda_m$, which is identical to Eq. (15). In the forecast model (boosted frame) the same wave is faster, and consequently, its travel time to 1 AU is shorter by the chosen offset time, Δt_0 :

$$t_{\text{travel}} = \frac{1 \text{ AU} - R_{\text{SC/IH}}}{\lambda^{(\ell)}/(1 - \lambda^{(\ell)}/\Lambda_m)} = \frac{1 \text{ AU} - R_{\text{SC/IH}}}{\lambda^{(\ell)}} - \Delta t_0 \quad (18)$$

These considerations allows us to present an analytical solution of the one-dimensional (1-D) Riemann problem for the hydrodynamic equations with the discontinuous initial conditions: flow with constant parameters for $0 \leq x < 0.5$, denoted below as the left state (subscript ‘‘L’’) and flow with a different set of constant parameters at $0.5 < x \leq 1$ denoted with subscript ‘‘R.’’ The time offset is zero at $0.5 \leq x \leq 1$ and it increases linearly with x for $x \geq 0.5$, reaching the value of $\Delta \tau_0$ at the right boundary. The evolution during $0 \leq t \leq \Delta \tau_0$ for $0 \leq x \leq 0.5$ is governed by the usual hydrodynamic equations, while for $0.5 \leq x \leq 1$ the modified governing equations, given by

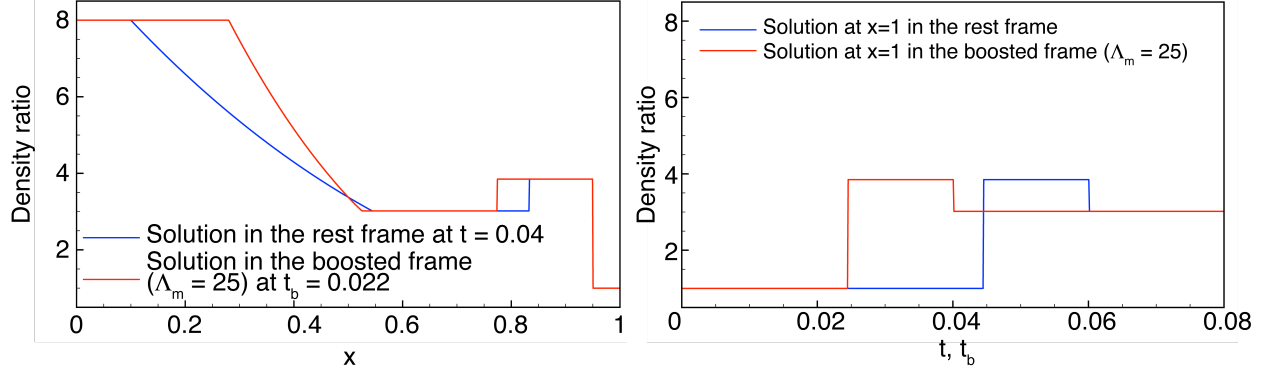


Figure 3: Solution of the Riemann problem with the initial condition: $\rho = 8$, $u = 0$ and $p = 480$ at $x < 0.5$; $\rho = 1$, $u = 0$ and $p = 1$ at $x > 0.5$, for a gas with $\gamma = 5/3$. **Left panel:** Blue line shows the solution of hydrodynamics equations in the rest frame at the time, $t = 0.04$; red line presents the solution in the boosted frame at time $t_b = 0.022$. **Right panel:** Time profile of density at $x = 1$. Red line is the solution in the boosted frame, blue line is the solution in the rest frame. $\rho(t_b)$ predicts the solution in the rest frame, $\rho(t)$ with the time offset of 0.02.

Eqs. (9), are used with $\Lambda_m = 0.5/\Delta\tau_0$.

In hydrodynamics, the solution of the Riemann problem for the set of *primitive variables*, $\mathcal{P} = [\rho, \mathbf{u}, p]^T$, that combines the density, velocity vector, and pressure, is known to be a *self-similar* function \mathcal{P}_{RS} , combining time and location, $(x - 0.5)/t$: $\mathcal{P} = \mathcal{P}_{\text{RS}}([x - 0.5]/t)$. In the linear approximation, the solution is composed of constant states separated by jump-like waves (the *simple* Riemann waves) propagating with the characteristic speeds from the initial location of the discontinuity at $x = 0.5$, i.e., the range of the self-similar argument for each constant state is $\lambda^{(\ell-1)} < (x - 0.5)/t < \lambda^{(\ell)}$. This solution of the Riemann problem can be applied as is for the region $0 \leq x \leq 0.5$. However, for $0.5 \leq x \leq 1$ the speeds of characteristic waves must be modified in accordance with Eq. (17), so that the self-similar argument of the \mathcal{P}_{RS} function needs to be modified accordingly:

$$\mathcal{P} = \begin{cases} \mathcal{P}_{\text{RS}}\left(\frac{x-0.5}{t_b}\right) & \text{if } 0 \leq x \leq 0.5 \\ \mathcal{P}_{\text{RS}}\left(\frac{x-0.5}{1 + \frac{1}{\Lambda_m} \frac{x-0.5}{t_b}}\right) & \text{if } 0.5 \leq x \leq 1. \end{cases} \quad (19)$$

This solution can be also applied to the solution of a non-linear Riemann problem with no loss of generality, because it can also be obtained from the known with a self-similar argument by applying spacetime transformation to the argument.

As an example Fig. 3 presents the solution of the Riemann problem for a gas with a polytropic index, $\gamma = 5/3$ with the following initial condition: $\rho = 8$, $u = 0$ and $p = 480$ at $0 \leq x < 0.5$; $\rho = 1$, $u = 0$ and $p = 1$ for $0.5 < x \leq 1$. In the left panel, the blue line shows the solution of hydrodynamic equations in the rest frame at time, $t = 0.04$. At this time, the rarefaction wave propagating to the left reaches $x = 0.1$, while the shock wave propagating to the right arrives at the “observation” point at $x = 0.95$ (note that the red and blue lines overlap beyond $x = 0.85$). The red line is the solution in the boosted frame, such that the time offset, $\Delta t(x)$ varies from zero at $x \leq 0.5$ to $\Delta t_0 = 0.02$ at $x = 1$ (which corresponds to $\Lambda_m = (1 - 0.5)/0.02 = 25$) for the time instant, $t_b = 0.022$. At $x \leq 0.5$ (with no time offset) the rarefaction wave passes a much shorter

distance during the shorter time interval, $0.022 < 0.04$. However, the time offset at $x = 0.95$ is $(0.95 - 0.5)/\Lambda_m = 0.018$, therefore, the shock arrival time in the boosted frame plus the time offset equals to the shock arrival time at the rest frame $0.04 = 0.022 + 0.018$. The right panel presents the time dependence of density at $x = 1$ in the rest frame (blue line) and in the boosted frame (red line). Comparing the results clearly demonstrates the time offset ($= 0.02$).

4.2. Speed of Arbitrarily Directed Characteristic Linear Waves

For linear waves propagating in an arbitrary direction (not necessarily radially) we can use their property of *phase invariance*, well-known for *harmonic waves*. Consider a perturbation of primitive variables, $\delta\mathcal{P}$ in the rest frame which depends on coordinates and time via the harmonic factor, $\delta\mathcal{P} \propto \text{Re} \{ \exp [i (\mathbf{k} \cdot \mathbf{x} - \omega t)] \}$, i being the imaginary unit, \mathbf{k} being the wave vector and ω being its frequency.

The vector of characteristic perturbation velocities, $\boldsymbol{\lambda}^{(\ell)}$, can be expressed via the wave vector and frequency: $\omega = \boldsymbol{\lambda}^{(\ell)} \cdot \mathbf{k}$, $\boldsymbol{\lambda}^{(\ell)} = \partial\omega/\partial\mathbf{k}$. The phase invariance (see, e.g., [Landau and Lifshitz, 1975](#)) means that in the (Lorenz) boosted frame the wave phase does not change once expressed in terms of the wave vector, \mathbf{k}_b and frequency, ω_b in the transformed spacetime: $\mathbf{k} \cdot \mathbf{x} - \omega t = \mathbf{k}_b \cdot \mathbf{x}_b - \omega_b t_b$. From this equation, with the help of Eq. (3), we can find the wave vector and frequency in the boosted frame:

$$\omega_b = \omega, \quad \mathbf{k}_b = \mathbf{k} - \frac{\omega}{\Lambda_m} \hat{\mathbf{e}}_R, \quad \mathbf{k} = \mathbf{k}_b + \frac{\omega}{\Lambda_m} \hat{\mathbf{e}}_R, \quad (20)$$

while the perturbation velocity in the boosted frame can be found from the following identity:

$$\boldsymbol{\lambda}_b^{(\ell)} = \frac{\partial\omega_b}{\partial\mathbf{k}_b} = \frac{\partial\omega}{\partial\mathbf{k}_b} = \frac{\partial\omega}{\partial\mathbf{k}} \cdot \frac{\partial\mathbf{k}}{\partial\mathbf{k}_b} = \boldsymbol{\lambda}^{(\ell)} \cdot \frac{\partial \left(\mathbf{k}_b + \hat{\mathbf{e}}_R \frac{\omega_b}{\Lambda_m} \right)}{\partial\mathbf{k}_b} = \boldsymbol{\lambda}^{(\ell)} + \frac{\hat{\mathbf{e}}_R \cdot \boldsymbol{\lambda}^{(\ell)}}{\Lambda_m} \boldsymbol{\lambda}_b^{(\ell)}, \quad (21)$$

giving:

$$\boldsymbol{\lambda}_b^{(\ell)} = \frac{\boldsymbol{\lambda}^{(\ell)}}{1 - \frac{\hat{\mathbf{e}}_R \cdot \boldsymbol{\lambda}^{(\ell)}}{\Lambda_m}} \quad (22)$$

One of the examples of ‘‘characteristic perturbations’’ is the contact discontinuity bounding the ‘‘magnetic cloud’’, which is believed to be one of the possible kinds of CMEs. Hence, once the CME is simulated in the boosted frame, its arrival time forecast can be obtained by the offset time, Δt_0 , ahead of real time.

5. Forecast System Based on the MHD Equations

To model the solar-terrestrial environment that is significantly affected by the solar, interplanetary or planetary magnetic field, \mathbf{B} , a magnetohydrodynamics (MHD) model is used. While solving MHD equations, the system of conservation laws should be completed with the source

terms proportional to $\nabla \cdot \mathbf{B}$ (see [Powell et al., 1999](#)):

$$\frac{\partial}{\partial t} \begin{bmatrix} \rho \\ \rho \mathbf{u} \\ \mathbf{B} \\ \frac{\rho u^2}{2} + \frac{P}{\gamma-1} + \frac{B^2}{2\mu_0} \end{bmatrix} + \nabla \cdot \begin{bmatrix} \rho \mathbf{u} \\ \rho \mathbf{u} \mathbf{u} + \left(P + \frac{B^2}{2\mu_0} \right) \mathbf{I} - \frac{\mathbf{B}\mathbf{B}}{\mu_0} \\ \mathbf{u}\mathbf{B} - \mathbf{B}\mathbf{u} \\ \mathbf{u} \left(\frac{\rho u^2}{2} + \frac{\gamma P}{\gamma-1} + \frac{B^2}{\mu_0} \right) - \mathbf{B} \frac{\mathbf{u} \cdot \mathbf{B}}{\mu_0} \end{bmatrix} + \begin{bmatrix} 0 \\ \frac{\mathbf{B}}{\mu_0} \\ \mathbf{u} \\ \frac{\mathbf{u} \cdot \mathbf{B}}{\mu_0} \end{bmatrix} \nabla \cdot \mathbf{B} = 0. \quad (23)$$

This approach allows constructing a high-resolution numerical flux, including a non-degenerate “8th wave” flushing away non-zero $\nabla \cdot \mathbf{B}$, if any. In the next step we transform Eqs. (23) to a boosted frame using Eq. (8). In addition to the transformation of the flux divergence described above where we derived Eq. (9), the gradient operator at constant t in the $\nabla \cdot \mathbf{B}$ term should also be expressed in spacetime (t_b, \mathbf{x}) :

$$(\nabla \cdot \mathbf{B})_{t=\text{const}} = (\nabla \cdot \mathbf{B})_{t_b=\text{const}} - \frac{1}{\Lambda_m} \frac{\partial \hat{\mathbf{e}}_R \cdot \mathbf{B}}{\partial t_b}. \quad (24)$$

With these regards, in the boosted frame the revised Eq. (23) differs from Eq. (9) by the terms resulting from Eq. (24):

$$\frac{\partial}{\partial t_b} \left(U_i - \frac{1}{\Lambda_m} \hat{\mathbf{e}}_R \cdot \mathbf{F}_i \right) - \frac{1}{\Lambda_m} \frac{\partial \hat{\mathbf{e}}_R \cdot \mathbf{B}}{\partial t_b} \begin{bmatrix} 0 \\ \frac{\mathbf{B}}{\mu_0} \\ \mathbf{u} \\ \frac{\mathbf{u} \cdot \mathbf{B}}{\mu_0} \end{bmatrix} + \nabla \cdot \mathbf{F}_i + \begin{bmatrix} 0 \\ \frac{\mathbf{B}}{\mu_0} \\ \mathbf{u} \\ \frac{\mathbf{u} \cdot \mathbf{B}}{\mu_0} \end{bmatrix} \nabla \cdot \mathbf{B} = 0, \quad (25)$$

where, for brevity, we use index notations, U_i and \mathbf{F}_i , for the conserved variables and their fluxes as explicitly defined in Eq. (23).

6. Numerical Example for Solar Wind Forecast

As a proof of principle, we simulated the CME propagation in the rest frame and boosted frame. We employed the settings recently used by [Liu et al. \(2024\)](#) to model the April 11, 2014 CME event. We simulate SC with the Alfvén wave turbulence driven solar atmosphere model (AWSO-M-R) as described in [Sokolov et al. \(2021\)](#). However, for the IH domain we used simplified MHD model of Sec. 5 accomplished with adiabatic Eq. (D.2) for electron pressure, with no turbulence.

Ambient (background) state in the coupled SC and IH models is obtained as a steady-state solution of the stream-aligned MHD equations by [Sokolov et al. \(2022\)](#). Then we applied the Eruptive event generator using Gibson-Low configuration (EEGGL, see [Borovikov et al., 2017](#), and references cited therein). We simulated the CME propagation in the rest frame for $t = 32$ hours of physical time after the CME onset. The resulting state in the IH for the final time is presented in the left panel of Fig. (4). White color lines are the magnetic field lines and color bar shows the distribution of radial solar wind speed, in the solar equatorial plane, i.e., xy -coordinate plane of the HGR coordinate system. It can be seen that at $t \approx 32$ hours the CME-driven shock reaches the Earth location (shown by the green asterisk).

In the right panel we provide the result of simulation, in which the SC is modeled in the rest frame, however, in the IH the boosted frame is used. The panel shows a xy -plane of HGR coor-

dinates at the time $t_b = 16$ hours after the CME onset.

With the choice of the time offset of $\Delta t_0 = 25$ hours at 1 AU, the scheme described in Appendix is applicable for the most time of simulation, however, at the time of $t_b \approx 2 - 4$ hours the plasma radial speed exceeds $1600 \text{ km/s} > \Lambda_m \approx 1500 \text{ km/s}$. The best choice of time offset to simulate this event in the boosted frame appears to be $\Delta t_0 = 16$ hours. The maximum boost factor is as high as $\Gamma_B \geq 10$ at $t_b \approx 2$, which means that maximum radial speed of perturbation, $c_{R_{\max}}$ is very close to Λ_m . With the chosen time offset, although the data at 0.1 AU (shown by dashed circle) correspond to the physical time $t = t_b = 16$ hours, at the heliospheric distance of 0.55 AU (shown by dotted line, the half of offset time is added, hence, the data correspond to time of $t = t_b + \Delta t_0/2 = 24$ hours after the CME onset. At 1 AU shown by solid circle, the simulated parameters correspond to the physical time with the full time offset, $t = t_b + \Delta t_0 = 32$ hours, and these data clearly demonstrate the shock wave arrival to the Earth location (green star) at $t = 32 \text{ km/s}$.

Thus, in the presented numerical test the result for the shock wave arrival time is obtained in two ways, in the traditional (rest frame) and newly suggested (boosted frame) ones. Both approaches provide identical predictions for results at 1 AU, thus justifying both the quantitative accuracy of the new method and reliability of the numerical algorithms described in the Appendices.

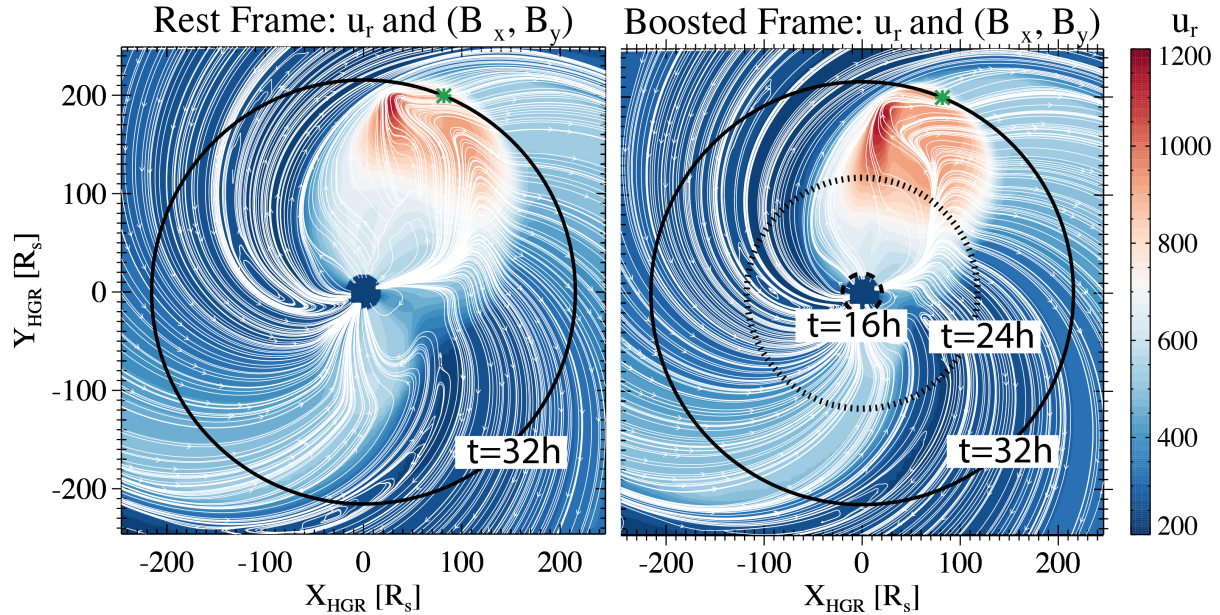


Figure 4: Left panel: Snapshot of the time accurate solution in the rest frame 32 hours after the CME onset; Right panel: Boosted frame solution at $t_b = t - \frac{16}{0.9}(R - 0.1)$ ($[t]=\text{h}$, $[R]=\text{AU}$). The plasma and IMF parameters at the concentric circles represent solutions at $t=16\text{h}$, 24h and 32h after CME onset. Earth's location is marked by a green star. The two solutions are identical at 1AU (the $t=32\text{h}$ circle), but differ at all other distances. Note that the boosted solution at 1AU is 16h ahead of the solution at the SC/SH boundary.

7. Conclusions

An important distinctive feature of the proposed approach is that the simulation in the SC is driven by hourly updated solar magnetograms and is continuously simulated in nearly real time.

The predictive capability for the solar wind and IMF parameters at 1 AU is achieved with using the time offset, such that current observations of the solar magnetic field are simulated simultaneously with tomorrow's parameters of the ambient solar wind at 1 AU. In the numerical test for transient propagation, the boosted solution for the CME-driven shock arrival at 1AU is 16h ahead of the solution at the SC/IH boundary.

8. Acknowledgements

The authors are grateful Maria M. Kuznetsova (NASA GSFC) for stimulating our interest to the space weather forecast problem and acknowledge discussions with Gabor Toth and Lulu Zhao as well as the help of Weihao Liu with visualization. This research is partially based upon work supported by a NASA LWS Strategic Capability (SCEPTER) project at the University of Michigan under NASA grant 80NSSC22K0892, by a NASA LWS Space Weather Centers of Excellence project (CLEAR) at the University of Michigan under NASA grant 80NSSC23M0191, by NASA grant 80NSSC21K1124, by NSF ANSWERS grant GEO-2149771 and by NASA LWS grant 80NSSC20K1778. We would also like to acknowledge high-performance computing support from: (1) Yellowstone provided by NCAR's Computational and Information Systems Laboratory, sponsored by the NSF, and (2) Pleiades operated by NASA's Advanced Supercomputing Division.

References

- Arge, C., Henney, C., Gonzalez-Hernandez, I., Toussaint, W., Koller, J., Godinez, H., 2013. Modeling the corona and solar wind using ADAPT maps that include far-side. *Solar Wind 13*, AIP Conf. Series 1539, 11–14.
- Arge, C.N., Henney, C.J., Koller, J., Toussaint, W.A., Harvey, J.W., Young, S., 2011. Improving data drivers for coronal and solar wind models. *ASTRONUM 2010*, ASP Conference Series 44.
- Borovikov, D., Sokolov, I.V., Manchester, W.B., Jin, M., Gombosi, T.I., 2017. Eruptive event generator based on the Gibson-Low magnetic configuration. *Journal of Geophysical Research (Space Physics)* 122, 7979–7984. doi:doi:10.1002/2017JA024304, arXiv:1708.01635.
- Brio, M., Wu, C.C., 1988. An upwind differencing scheme for the equations of ideal magnetohydrodynamics. *J. Comp. Phys.* 75, 400–422. doi:doi:10.1016/0021-9991(88)90120-9.
- Cargo, P., Gallice, G., 1997. Roe matrices for ideal mhd and systematic construction of roe matrices for systems of conservation laws. *Journal of Computational Physics* 136, 446–466. URL: <https://www.sciencedirect.com/science/article/pii/S0021999197957739>, doi:doi:https://doi.org/10.1006/jcph.1997.5773.
- Falle, S.A.E.G., Komissarov, S.S., 1996. An upwind numerical scheme for relativistic hydrodynamics with a general equation of state. *Monthly Notices of the Royal Astronomical Society* 278, 586–602. URL: <https://doi.org/10.1093/mnras/278.2.586>, doi:doi:10.1093/mnras/278.2.586.

- Gombosi, T., Chen, Y., Glocer, A., Huang, Z., Jia, X., Liemohn, M.W., Manchester, W., Pulkkinen, T., Sachdeva, N., Shidi, Q.A., Sokolov, I., Szente, J., Tenishev, V., Toth, G., van der Holst, B., Welling, D., Zhao, L., Zou, S., 2021. What sustained multi-disciplinary research can achieve: The Space Weather Modeling Framework. *Journal of Space Weather and Space Climate* 11, 41. doi:doi:[10.1051/swsc/2021020](https://doi.org/10.1051/swsc/2021020).
- Hirsch, C., 1997. Numerical computation of internal and external flows. John Wiley & Sons, Chichester [England].
- Landau, L., Lifshitz, E., 1975. The Classical Theory of Fields. volume 2 of *Course of Theoretical Physics*. 4th ed., Pergamon, Amsterdam. doi:doi:<https://doi.org/10.1016/B978-0-08-025072-4.50008-3>.
- Landau, L.D., Lifshitz, E.M., 1959. Fluid mechanics. Course of theoretical physics, Oxford: Pergamon Press, 1959.
- van Leer, B., . Upwind and High-Resolution Methods for Compressible Flow: From Donor Cell to Residual-Distribution Schemes. URL: <https://arc.aiaa.org/doi/abs/10.2514/6.2003-3559>, doi:doi:[10.2514/6.2003-3559](https://doi.org/10.2514/6.2003-3559), arXiv:<https://arxiv.org/abs/https://arc.aiaa.org/doi/pdf/10.2514/6.2003-3559>.
- Liu, W., Sokolov, I.V., Zhao, L., Gombosi, T.I., Chen, X., Sachdeva, N., Tóth, G., Manchester, IV, W.B., Lario, D., Whitman, K., Bruno, A., Cohen, C.M.S., Mays, M.L., Bain, H.M., 2024. Physics-Based Simulation of the 2013 April 11 SEP Event. arXiv e-prints , arXiv:2412.07581doi:doi:[10.48550/arXiv.2412.07581](https://doi.org/10.48550/arXiv.2412.07581), arXiv:[2412.07581](https://arxiv.org/abs/2412.07581).
- Odstrčil, 2003. Modeling 3-D solar wind structure. *Adv. Space Sci.* 32, 497–506. doi:doi:[10.1029/2004JA010745](https://doi.org/10.1029/2004JA010745).
- Odstrčil, D., Pizzo, V.J., 1999a. Three-Dimensional Propagation of Coronal Mass Ejections in a Structured Solar Wind Flow 1. CME Launched Within the Streamer Belt. *J. Geophys. Res.* 104, 483–492.
- Odstrčil, D., Pizzo, V.J., 1999b. Three-Dimensional Propagation of Coronal Mass Ejections in a Structured Solar Wind Flow 2. CME Launched Adjacent to the Streamer Belt. *J. Geophys. Res.* 104, 493–504. doi:doi:[10.1029/1998JA900038](https://doi.org/10.1029/1998JA900038).
- Powell, K.G., Roe, P.L., Linde, T.J., Gombosi, T.I., De Zeeuw, D.L., 1999. A Solution-Adaptive Upwind Scheme for Ideal Magnetohydrodynamics. *Journal of Computational Physics* 154, 284–309. doi:doi:[10.1006/jcph.1999.6299](https://doi.org/10.1006/jcph.1999.6299).
- Shore, S.N., 1992. Chapter 6 - magnetic fields in astrophysics, in: *An Introduction to Astrophysical Hydrodynamics*. Academic Press, San Diego, pp. 171 – 213.
- Sokolov, I., Zhang, H.M., Sakai, J., 2001. Simple and efficient godunov scheme for computational relativistic gas dynamics. *Journal of Computational Physics* 172, 209–234. URL: <https://www.sciencedirect.com/science/article/pii/S0021999101968214>, doi:doi:<https://doi.org/10.1006/jcph.2001.6821>.

- Sokolov, I.V., Timofeev, E.V., ichi Sakai, J., Takayama, K., 2002. Artificial wind—a new framework to construct simple and efficient upwind shock-capturing schemes. *Journal of Computational Physics* 181, 354–393. URL: <https://www.sciencedirect.com/science/article/pii/S0021999102971305>, doi:doi:<https://doi.org/10.1006/jcph.2002.7130>.
- Sokolov, I.V., van der Holst, B., Manchester, W.B., Ozturk, D.C.S., Szente, J., Taktakishvili, A., Tóth, G., Jin, M., Gombosi, T.I., 2021. Threaded-field-lines model for the low solar corona powered by the Alfvén wave turbulence. *The Astrophysical Journal* 908, 172–183.
- Sokolov, I.V., van der Holst, B., Oran, R., Downs, C., Rousev, I.I., Jin, M., Manchester, IV, W.B., Evans, R.M., Gombosi, T.I., 2013. Magnetohydrodynamic Waves and Coronal Heating: Unifying Empirical and MHD Turbulence Models. *The Astrophysical Journal* 764, 23. doi:doi:[10.1088/0004-637X/764/1/23](https://doi.org/10.1088/0004-637X/764/1/23), [arXiv:1208.3141](https://arxiv.org/abs/1208.3141).
- Sokolov, I.V., Zhao, L., Gombosi, T.I., 2022. Stream-aligned magnetohydrodynamics for solar wind simulations. *The Astrophysical Journal* 926, 102. doi:doi:[10.3847/1538-4357/ac400f](https://doi.org/10.3847/1538-4357/ac400f).
- Toro, E., 2009. *Riemann Solvers and Numerical Methods for Fluid Dynamics: A Practical Introduction*. Springer Berlin Heidelberg. URL: <https://books.google.com/books?id=SqEjX0um8o0C>.
- Tóth, G., Sokolov, I.V., Gombosi, T.I., Chesney, D.R., Clauer, C.R., De Zeeuw, D.L., Hansen, K.C., Kane, K.J., Manchester, W.B., Oehmke, R.C., Powell, K.G., Ridley, A.J., Rousev, I.I., Stout, Q.F., Volberg, O., Wolf, R.A., Sazykin, S., Chan, A., Yu, B., Kóta, J., 2005. Space Weather Modeling Framework: A new tool for the space science community. *Journal of Geophysical Research (Space Physics)* 110, A12226. doi:doi:[10.1029/2005JA011126](https://doi.org/10.1029/2005JA011126).
- van der Holst, B., Sokolov, I.V., Meng, X., Jin, M., Manchester, W.B., Toth, G., Gombosi, T.I., 2014. Alfvén Wave Solar Model (AWSoM): Coronal Heating. *Astrophys. J.* 782, 81. doi:doi:[10.1088/0004-637x/782/2/81](https://doi.org/10.1088/0004-637x/782/2/81), [arXiv:1311.4093](https://arxiv.org/abs/1311.4093).

Appendix A. Finite Volume Formulation of Boosted Conservation Laws

Appendix A.1. Discretization

One of the most important examples of the system of conservation laws are the hydrodynamic equations. Computational Fluid Dynamics (CFD) has been developed to be a powerful applied science employing a variety of numerical methods, reviewed by [Hirsch \(1997\)](#). Among them is the widely used *finite volume approach*. Once the system of equations given by Eq. (6) is integrated over a *control volume*, ΔV , the integral of the term, $\nabla \cdot \mathbf{F}$, in each equation reduces to a surface integral of the flux function over the boundary of the control volume:

$$\int_{\Delta V} (\nabla \cdot \mathbf{F}) d^3\mathbf{x} = \int_{\sigma} \mathbf{F} \cdot d\boldsymbol{\sigma} \quad (\text{A.1})$$

If the *computational domain* of the conservation-law system is decomposed into a set of control volumes (*cells*), ΔV_i , the time evolution of the conserved variable within each control volume

reduces to the exchange by the *numerical fluxes* between each pair of neighboring cells, i th and j th:

$$\frac{d}{dt} \int_{\Delta V_i} U(t, \mathbf{x}) d^3\mathbf{x} = - \sum_j \mathbf{F}_{ij} \cdot \boldsymbol{\sigma}_{ij} \quad (\text{A.2})$$

The numerical fluxes $\mathbf{F}_{ij} \cdot \boldsymbol{\sigma}_{ij}$, are essentially the integrals of the flux function, \mathbf{F} , over the interface (the shared boundary) of two neighboring cells. Gauss' theorem (Eq. A.1) is formulated via the dot product of the flux function with the “external” unit vector of the boundary surface for i th cell, which is at the same time the negative of the “external” unit vector to the same interface for j th neighboring cell, so that the numerical flux from i th cell to j th cell is always equal to the negative of the flux from j th cell to i th cell, therefore, $\boldsymbol{\sigma}_{ji} = -\boldsymbol{\sigma}_{ij}$. Consequently, the time derivative of the total integral of the conserved quantity over the computational domain, given by the sum of Eqs. (A.2) over all control volumes, reduces to mutually canceling contributions from each numerical flux to the neighboring cells, resulting in the automatically conserved total physical quantities such as mass, momentum and energy, unless there is a non-vanishing flux of these quantities through the external boundary of the computational domain. Such schemes are well known as *conservative numerical schemes*. In terms of the averages of conserved variables, over the i th control volume at sequentially increasing time levels with a time-step of Δt ,

$$U_i^n = \frac{1}{\Delta V_i} \int_{\Delta V_i} U(t = t^n, \mathbf{x}) d^3\mathbf{x}, \quad (\text{A.3})$$

where the superscript, n , denotes variables related to time $t = t^n$, and the numerical scheme becomes:

$$U_i^{n+1} = U_i^n - \frac{\Delta t}{\Delta V_i} \sum_j \mathbf{F}_{ij} \cdot \boldsymbol{\sigma}_{ij} \quad (\text{A.4})$$

In applying this approach to Eq. (7) in the SC part of computational domain, we directly solve for U_i^{n+1} ,

$$U_i^{n+1} = U_i^n - \frac{\Delta t_b}{\Delta V_i} \sum_j \mathbf{F}_{ij} \cdot \boldsymbol{\sigma}_{ij}, \quad R < R_{\text{SC/IH}}. \quad (\text{A.5})$$

However, in the boosted IH domain to solve Eq. (9), we need to choose a special form of the 4-D control volume (see Fig. A.5), in which n th state at $t_b = t^n$ in the boosted frame corresponds to the *hyper-surface* $t - (\|\mathbf{x}\| - R_{\text{SC/IH}})/\Lambda_m = t^n$ in the 4-D rest frame, (t, \mathbf{x}) (blue dashed line in Fig. A.5). Integrating Eq. (9) over control volume and over t_b gives the finite volume formulation as follows:

$$\tilde{U}_i^{n+1} = \tilde{U}_i^n - \frac{\Delta t_b}{\Delta V_i} \sum_j \mathbf{F}_{ij} \cdot \boldsymbol{\sigma}_{ij}, \quad R > R_{\text{SC/IH}}, \quad (\text{A.6})$$

where the conserved quantity is modified as follows:

$$\tilde{U}_i^n = \frac{1}{\Delta V_i} \int_{\Delta V_i} \tilde{U}(t_b = t^n, \mathbf{x}) d^3\mathbf{x}, \quad \tilde{U} = U - \frac{\hat{\mathbf{e}}_R \cdot \mathbf{F}}{\Lambda_m}. \quad (\text{A.7})$$

There is an alternative way to derive Eqs. (A.6) and (A.7) by applying Gauss' theorem to Eq. (6),

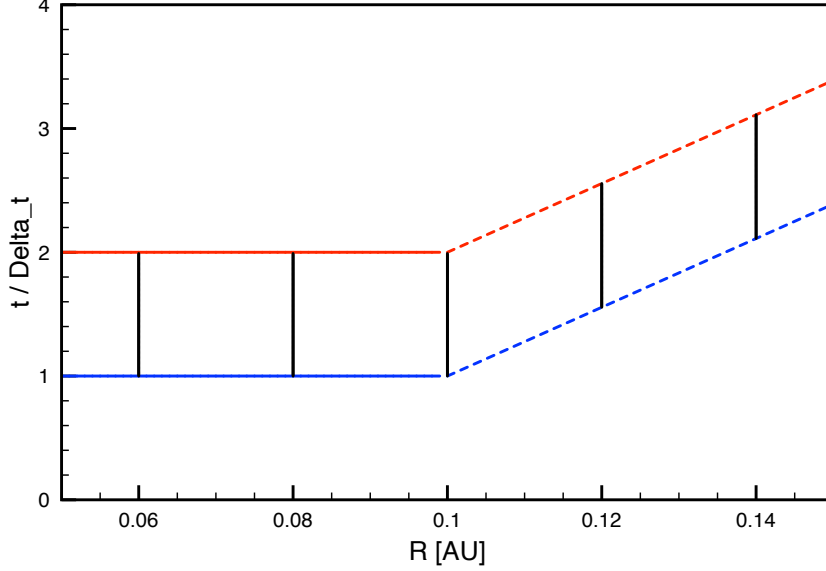


Figure A.5: 4-D control volumes used in the Lorentz boosted frame computations on the $R - t$ diagram. Vertical lines show the spatial immovable boundaries of the control volumes. In the SC domain, $R < 0.1$ AU, the time in the boosted frame coincides with that of in the rest frame and at the time levels of constant t_b , $t_b = t^n$ (horizontal solid blue line) and $t_b = t^{n+1}$ (horizontal solid red line) the real time is also constant, $t = t^n$ and $t = t^{n+1}$. In the IH model, at time levels $t_b = t^n$ (blue dashed line) and $t_b = t^{n+1}$ (red dashed line), the real time is not constant and the dashed lines are not parallel to the horizontal direction.

which can be considered as an equation for a divergence-free 4-vector, $(\frac{\partial}{\partial t}, \frac{\partial}{\partial \mathbf{x}}) \cdot (U, \mathbf{F}) = 0$. The integral of this 4-D divergence over the 4-D control volume shown in Fig. A.5 reduces to an integral over hyper-surfaces bounding the control volume. Since the hyper-surfaces, shown by blue and red dashed lines in Fig. A.5 are no longer orthogonal to the t -axis, the integrand over these hyper-surfaces is no longer equal to U , but to a linear combination of U and $F_R = \hat{\mathbf{e}}_R \cdot \mathbf{F}$. Similarly, if the (numerical) flux is calculated in the frame of reference moving with a velocity of Λ , or if the control volume moves, the spatial boundary of the control volume is no longer parallel to the direction of t -axis, resulting in the modification of the flux function ($F \rightarrow F - \Lambda U$ in the 1-D case (e.g., Sokolov et al., 2002)).

Eqs. (A.5) and (A.6) constitute an almost complete solution algorithm, since the computation of numerical flux is the most laborious and time-consuming part of the numerical scheme and this part is taken with no modification from the standard control volume approach. Specifically, an existing finite volume code can be easily converted for solar wind forecast. In addition to simplified computation, the use of identical numerical fluxes in the rest frame and in the boosted frame ensures the equivalence of a steady-state “ambient” solution for the solar wind in the coordinate frame co-rotating with the Sun regardless of the frame in which it is obtained. Indeed, the numerical solution, obtained in the rest frame with the numerical scheme given by Eq. (A.4) describes steady-state, $U_i^{n+1} \equiv U_i^n$ for all conserved variables in all cells, if, and only if $\frac{1}{\Delta V_i} \sum_j \mathbf{F}_{ij} \cdot \boldsymbol{\sigma}_{ij} \equiv 0$. As long as the same numerical fluxes are used in the numerical scheme given by Eq. (A.6) in the boosted frame, the solution is also steady-state, since $\tilde{U}_i^{n+1} \equiv \tilde{U}_i^n$. There are, however, two differences to be addressed when the boosted frame is used: the recovery of primitive variables from the modified conservative ones and the modification of the Courant condition on the time step caused

by the modification of the characteristic wave speed.

Appendix A.2. Recovery of Primitive Variables

Once the state vector is known at $t_b = t^n$ and the numerical fluxes are calculated, Eq. (A.6) allows us to obtain the modified conserved variable, \tilde{U}_i^{n+1} . However, unlike in the case of standard conserved variables, it is not easy to recover the physical quantities, \mathcal{P}_i^{n+1} , from the known modified conserved variables. One of the reasons is the non-linear dependence of \tilde{U}^{n+1} on the radial component of the solar wind velocity, $u_R^{n+1} = \hat{\mathbf{e}}_R \cdot \mathbf{u}^{n+1}$. Indeed, as this velocity determines the radial component of momentum density, it is a part of some component of U^{n+1} . At the same time the flux projection on the radial direction, $(\hat{\mathbf{e}}_R/\Lambda_m) \cdot \mathbf{F}^{n+1}$ usually includes the advection term, $(u_R^{n+1}/\Lambda_m)U^{n+1}$, so that u_R^{n+1} is also a part of all modified conserved variables thus making it challenging to derive.

A similar problem is well-known in relativistic computational hydrodynamics (see, e.g., [Falle and Komissarov, 1996](#); [Sokolov et al., 2001](#)) where the relativistic Γ -dependence of both the density and the energy-momentum tensor components make the equation for velocity highly implicit. At this time there are two published ways to handle this issue. One of these is an iterative procedure to solve the primitive variables, \mathcal{P}_i^{n+1} (see, e.g. [Falle and Komissarov, 1996](#), “there is no difficulty in devising an efficient iterative procedure”, p. 589). The most generic way to iterate $\mathcal{P}_i^{(n+1,h)}$, $h = 0, 1, 2 \dots$ is by starting the iterative process with the value at time level t^n : $\mathcal{P}_i^{(n+1,0)} = \mathcal{P}_i^n$. Successive iterations can be found by re-writing the difference in the modified conserved variables in Eqs. (A.5) in the form of elements of an infinite series:

$$\sum_{h=0}^{\infty} \left[\tilde{U} \left(\mathcal{P}_i^{(n+1,h+1)} \right) - \tilde{U} \left(\mathcal{P}_i^{(n+1,h)} \right) \right] = -\frac{\Delta t_b}{\Delta V_i} \sum_j \mathbf{F}_{ij} \cdot \boldsymbol{\sigma}_{ij}, \quad (\text{A.8})$$

$$\mathcal{P}_i^{(n+1,0)} = \mathcal{P}_i^n, \quad \mathcal{P}_i^{(n+1,\infty)} = \mathcal{P}_i^{n+1}.$$

In each step of the iteration procedure, the equations are solved as follows:

$$\tilde{U} \left(\mathcal{P}_i^{(n+1,h+1)} \right) - \tilde{U} \left(\mathcal{P}_i^{(n+1,h)} \right) = \Delta^h, \quad (\text{A.9})$$

where

$$\Delta^h = \begin{cases} -\frac{\Delta t_b}{\Delta V_i} \sum_j \mathbf{F}_{ij} \cdot \boldsymbol{\sigma}_{ij}, & h = 0 \\ \Delta^{h-1} + \tilde{U} \left(\mathcal{P}_i^{(n+1,h-1)} \right) - \tilde{U} \left(\mathcal{P}_i^{(n+1,h)} \right), & h \geq 1 \end{cases} \quad (\text{A.10})$$

The left hand side (LHS) of Eqs. (A.9) can be approximately linearized as

$$\tilde{U} \left(\mathcal{P}_i^{(n+1,h+1)} \right) - \tilde{U} \left(\mathcal{P}_i^{(n+1,h)} \right) \approx \frac{\partial \tilde{U} \left(\mathcal{P}_i^{(n+1,h)} \right)}{\partial \mathcal{P}_i^{(n+1,h)}} \cdot \delta^{h+1} \mathcal{P}_i \quad (\text{A.11})$$

where $\delta^{h+1} \mathcal{P}_i = \mathcal{P}_i^{(n+1,h+1)} - \mathcal{P}_i^{(n+1,h)}$. The set of the linearized Eqs. (A.9) for each conserved

variable constitutes the full system of linear equations to solve² for $\delta^{h+1}\mathcal{P}_i$ and then to find the next iteration of primitive variables:

$$\mathcal{P}_i^{(n+1,h+1)} = \mathcal{P}_i^{(n+1,h)} + \delta^{h+1}\mathcal{P}_i. \quad (\text{A.12})$$

Note, that it may be beneficial to start the iterative procedure from different set of primitive variables, e.g., such that $U\left(\mathcal{P}_i^{(n+1,0)}\right) = U\left(\mathcal{P}_i^n\right) - \frac{\Delta t_b}{\Delta V_i} \sum_j \mathbf{F}_{ij} \cdot \boldsymbol{\sigma}_{ij}$, or the intermediate state as described in [Appendix A.3](#). An alternative choice results in extra terms, $\tilde{U}\left(\mathcal{P}_i^n\right) - \tilde{U}\left(\mathcal{P}_i^{(n+1,0)}\right)$, in the RHS of Eq. (A.8) as well as in Eq. (A.10) for $h = 0$.

Another way to solve for the physical quantities is to seek special cases where the primitive variables can be solved from a single algebraic equation. For example, [Sokolov et al. \(2001\)](#) showed that a special choice of the equation of state allows recovering the primitive variables from the conservative ones in relativistic hydrodynamics by solving a quadratic equation. Similarly, for the forecast system based on the 3-D hydrodynamic equations in the boosted frame, the change in pressure through the time step, $p^{n+1} - p^n$, can be solved from a quadratic equation, as we demonstrate in [Appendix B](#).

Appendix A.3. Revised Courant Condition

For a 1-D problem the Courant condition for stability of the numerical algorithm is straightforward. It is controlled by the maximum perturbation speed c_{\max} . In the rest frame the time step, Δt , cell size, Δx_i , and the maximum perturbation speed in each cell, $c_{(\max,i)}$, should satisfy the condition as follows:

$$\frac{\Delta t c_{(\max,i)}}{\Delta x_i} = \text{CFL} < 1, \quad (\text{A.13})$$

where CFL is the local value of Courant-Friedrichs-Levi (CFL) number. With the choice of global CFL number (should be less than one), the time step for stable computations in the rest frame can be calculated as follows:

$$\Delta t = \text{CFL} \min_i \left(\frac{\Delta x_i}{c_{(\max,i)}} \right). \quad (\text{A.14})$$

For 1-D solution on spherical grid in the boosted frame this formula should be modified in accordance with Eq. (17) for the maximum radial perturbation speed, $c_{R(\max,i)}$:

$$\Delta t_b = \text{CFL} \min_i \left[\left(\frac{\Delta x_i}{c_{R(\max,i)}} \right) \left(1 - \frac{c_{R(\max,i)}}{\Lambda_m} \right) \right]. \quad (\text{A.15})$$

This time step is positive as long as Ineq. (5) holds. Comparing with the Courant condition in the rest frame, the minimal allowed time step in each cell should be reduced by a factor of $1 - \frac{c_{R(\max,i)}}{\Lambda_m}$.

However, for 3-D problem such local estimate is both not convincing and impractical. More

²In [Appendix C.2](#) we present a simple and explicit solution for $\delta^{h+1}u_R$ satisfying this system

reliable approach is to minimize the factors in Eq. (A.15) *separately*:

$$\Delta t_b = \text{CFL} \min_i \left(\frac{\Delta x_i}{c_{R(\max,i)}} \right) \min_i \left(1 - \frac{c_{R(\max,i)}}{\Lambda_m} \right) = \frac{\Delta t}{\Gamma_B}, \quad (\text{A.16})$$

where we used Eq. (A.14) for time step in the rest frame and introduced *boost factor* (somewhat similar to the Lorentz Γ -factor):

$$\Gamma_B = \frac{1}{1 - \frac{c_{R\max}}{\Lambda_m}}, \quad c_{R\max} = \max_i \left(c_{R(\max,i)} \right). \quad (\text{A.17})$$

The larger is the boost factor, the closer is Λ_m to $c_{R\max}$, the longer is the forecast time allowed. Eqs. (A.16) are convenient to use within any available MHD model/code, since the time step, Δt , is calculated as usual (as if the simulation is done in the rest frame), but before application it should be divided by the separately calculated boost factor. In 3-D realistic case, the stability of the control volume scheme given by Eqs. (A.6 and A.7) can be justified in the following way. Let us assume that the state at the time level, $n + 1$, is calculated in two stages. Initially, the approximation, \bar{U}_i^{n+1} for conserved variables at $n + 1$ time level is calculated as follows:

$$\bar{U}_i^{n+1} = U_i^n - \Gamma_B \frac{\Delta t_b}{\Delta V_i} \sum_j \mathbf{F}_{ij} \cdot \boldsymbol{\sigma}_{ij}. \quad (\text{A.18})$$

This is explicit scheme, which is conditionnaly stable as long as $\Gamma_B \Delta t_b = \Delta t$ is the time step in the rest frame satisfying the Courant condition. Using the relation, $\tilde{U} = \frac{U}{\Gamma_B} + \frac{1}{\Lambda_m} (c_{R\max} U - \hat{\mathbf{e}}_R \cdot \mathbf{F})$, Eqs. (A.6 and A.7) can be reduced to:

$$U^{n+1} + \frac{\Gamma_B}{\Lambda_m} (c_{R\max} U^{n+1} - \hat{\mathbf{e}}_R \cdot \mathbf{F}^{n+1}) = \bar{U}^{n+1} + \frac{\Gamma_B}{\Lambda_m} (c_{R\max} U^n - \hat{\mathbf{e}}_R \cdot \mathbf{F}^n). \quad (\text{A.19})$$

This equation may be interpreted as the implicit donor-cell scheme (see, e. g. [van Leer](#)): the fictive cell with the state, \bar{U}^{n+1} , receives the upwinded flux, $\frac{\Gamma_B}{\Lambda_m} (c_{R\max} U^n - \hat{\mathbf{e}}_R \cdot \mathbf{F}^n)$, from the donor cell, in which the state is U^n , and donates implicit upwinded flux, $\frac{\Gamma_B}{\Lambda_m} (c_{R\max} U^{n+1} - \hat{\mathbf{e}}_R \cdot \mathbf{F}^{n+1})$ to somewhere. The scheme is stable, if $c_{R\max}$ exceeds the maximum perturbation speed in all states, U^n , \bar{U}^{n+1} , and U^{n+1} . The iterative algorithm described below survives even if the boost factor, playing the role of the CFL number for the donor-cell scheme, is as high as $\Gamma_B \sim 10 - 30$. In this case $\frac{c_{R\max}}{\Lambda_m} \approx 0.95$, thus allowing a reasonably long forecast time, $\Delta t_0 \propto \frac{1}{\Lambda_m}$, even for faster CME.

Appendix B. Forecast System Based on the 3-D Hydrodynamic Equations

Appendix B.1. Governing Equations and their Discretization

The hydrodynamic motion is governed by the continuity equation, momentum vector conservation law, and energy scalar conservation law, which for a gas with constant γ read:

$$\begin{aligned}\frac{\partial \rho}{\partial t} &= -\nabla \cdot (\rho \mathbf{u}), \\ \frac{\partial (\rho \mathbf{u})}{\partial t} &= -\nabla \cdot [\rho \mathbf{u} \mathbf{u} + p \mathbf{I}], \\ \frac{\partial}{\partial t} \left(\frac{\rho u^2}{2} + \frac{p}{\gamma - 1} \right) &= -\nabla \cdot \left[\left(\frac{\rho u^2}{2} + \frac{\gamma p}{\gamma - 1} \right) \mathbf{u} \right].\end{aligned}\tag{B.1}$$

On applying the finite volume formalism Eq. (A.6), the numerical fluxes, $-\frac{1}{\Delta V_i} \sum_j \mathbf{F}_{ij} \cdot \boldsymbol{\sigma}_{ij}$ in the right hand side (RHS) of the above equations gives us the numerical sources of mass, S_ρ , momentum $\mathbf{S}_{\rho \mathbf{u}}$, and energy S_ξ ; herewith, the subscript index, i enumerating the control volumes, is omitted. The vectors of velocity and momentum density are conveniently split into the radial components and the ‘‘horizontal’’ components, perpendicular to the radial direction:

$$u_{\mathbf{R}} = \hat{\mathbf{e}}_{\mathbf{R}} \cdot \mathbf{u}, \quad \mathbf{u}_{\perp} = \mathbf{u} - u_{\mathbf{R}} \hat{\mathbf{e}}_{\mathbf{R}}, \quad S_{\rho u_{\mathbf{R}}} = \hat{\mathbf{e}}_{\mathbf{R}} \cdot \mathbf{S}_{\rho \mathbf{u}}, \quad \mathbf{S}_{\rho \mathbf{u}_{\perp}} = \mathbf{S}_{\rho \mathbf{u}} - S_{\rho u_{\mathbf{R}}} \hat{\mathbf{e}}_{\mathbf{R}}.\tag{B.2}$$

With these regards, Eqs. (A.6) for 3-D hydrodynamic Eqs. (B.1) give:

$$\begin{aligned}\tilde{U}_\rho^{n+1} &= \Delta t_b S_\rho + \tilde{U}_\rho^n, \quad \tilde{U}_\rho^n = \rho^n \left(1 - \frac{u_{\mathbf{R}}^n}{\Lambda_m} \right) \\ \tilde{U}_{\rho u_{\mathbf{R}}}^{n+1} &= \Delta t_b S_{\rho u_{\mathbf{R}}} + \tilde{U}_{\rho u_{\mathbf{R}}}^n, \quad \tilde{U}_{\rho u_{\mathbf{R}}}^n = \rho^n \left(1 - \frac{u_{\mathbf{R}}^n}{\Lambda_m} \right) u_{\mathbf{R}}^n - \frac{p^n}{\Lambda_m}, \\ \tilde{\mathbf{U}}_{\rho \mathbf{u}_{\perp}}^{n+1} &= \Delta t_b \mathbf{S}_{\rho \mathbf{u}_{\perp}} + \tilde{\mathbf{U}}_{\rho \mathbf{u}_{\perp}}^n, \quad \tilde{\mathbf{U}}_{\rho \mathbf{u}_{\perp}}^n = \rho^n \left(1 - \frac{u_{\mathbf{R}}^n}{\Lambda_m} \right) \mathbf{u}_{\perp}^n, \\ \tilde{U}_\xi^{n+1} &= \Delta t_b S_\xi + \tilde{U}_\xi^n, \quad \tilde{U}_\xi^n = \frac{\rho^n (\mathbf{u}^n)^2}{2} \left(1 - \frac{u_{\mathbf{R}}^n}{\Lambda_m} \right) + \frac{p^n}{\gamma - 1} \left(1 - \frac{\gamma u_{\mathbf{R}}^n}{\Lambda_m} \right).\end{aligned}\tag{B.3}$$

Appendix B.2. Solving for Primitive Variables

Let us denote the LHS of the first of Eqs. (5) as

$$\bar{\rho} = \rho^{n+1} \left(1 - \frac{u_{\mathbf{R}}^{n+1}}{\Lambda_m} \right) = \Delta t_b S_\rho + \rho^n \left(1 - \frac{u_{\mathbf{R}}^n}{\Lambda_m} \right)\tag{B.4}$$

and use it not only to eliminate the factor $\rho^{n+1} (1 - u_{\text{R}}^{n+1}/\Lambda_m) = \bar{\rho}$ from $\tilde{U}_{\rho u_{\text{R}}}^{n+1}$, $\tilde{U}_{\rho \mathbf{u}_{\perp}}^{n+1}$ and $\tilde{U}_{\varepsilon}^{n+1}$, but also to eliminate the factor, $\rho^n (1 - u_{\text{R}}^n/\Lambda_m) = \bar{\rho} - \Delta t_b S_{\rho}$, from $\tilde{U}_{\rho u_{\text{R}}}^n$, $\tilde{U}_{\rho \mathbf{u}_{\perp}}^n$ and $\tilde{U}_{\varepsilon}^n$:

$$\begin{aligned}\tilde{U}_{\rho u_{\text{R}}}^{n+1} &= \Delta t_b (S_{\rho u_{\text{R}}} - u_{\text{R}}^n S_{\rho}) + \tilde{U}_{\rho u_{\text{R}}}^n, & \tilde{U}_{\rho u_{\text{R}}}^n &= \bar{\rho} u_{\text{R}}^n - \frac{p^n}{\Lambda_m}, \\ \tilde{U}_{\rho \mathbf{u}_{\perp}}^{n+1} &= \Delta t_b (\mathbf{S}_{\rho \mathbf{u}_{\perp}} - \mathbf{u}_{\perp}^n S_{\rho}) + \tilde{U}_{\rho \mathbf{u}_{\perp}}^n, & \tilde{U}_{\rho \mathbf{u}_{\perp}}^n &= \bar{\rho} \mathbf{u}_{\perp}^n, \\ \tilde{U}_{\varepsilon}^{n+1} &= \Delta t_b \left(S_{\varepsilon} - \frac{\mathbf{u}^2}{2} S_{\rho} \right) + \tilde{U}_{\varepsilon}^n, & \tilde{U}_{\varepsilon}^n &= \frac{\bar{\rho} (\mathbf{u}^n)^2}{2} + \frac{P^n}{\gamma - 1} \left(1 - \frac{\gamma u_{\text{R}}^n}{\Lambda_m} \right),\end{aligned}\tag{B.5}$$

where we keep notation, \tilde{U} , for the *reduced* conserved variables, although the expressions for them are simplified. In the next step we want to find the primitive variables from Eqs. (B.5), i.e., the components of the velocity vector and pressure (the density is obtained below from Eq. (B.4), once u_{R}^{n+1} is known). The equation for the perpendicular velocity (the second equation in Eqs. B.5) can be solved explicitly:

$$\mathbf{u}_{\perp}^{n+1} = \frac{\Delta t_b}{\bar{\rho}} (\mathbf{S}_{\rho \mathbf{u}_{\perp}} - \mathbf{u}_{\perp}^n S_{\rho}) + \mathbf{u}_{\perp}^n.\tag{B.6}$$

Eq. (B.6) can be used to eliminate \mathbf{u}_{\perp}^2 from the energy equation (the third line in of Eqs. B.5), which now becomes:

$$\begin{aligned}\tilde{U}_{\varepsilon}^{n+1} &= \Delta t_b \left[S_{\varepsilon} - \frac{\mathbf{u}^2}{2} S_{\rho} - \mathbf{u}_{\perp}^n \cdot (\mathbf{S}_{\rho \mathbf{u}_{\perp}} - \mathbf{u}_{\perp}^n S_{\rho}) \right] - \frac{(\Delta t_b)^2}{2\bar{\rho}} (\mathbf{S}_{\rho \mathbf{u}_{\perp}} - \mathbf{u}_{\perp}^n S_{\rho})^2 + \tilde{U}_{\varepsilon}^n, \\ \tilde{U}_{\varepsilon}^n &= \frac{\bar{\rho} (u_{\text{R}}^n)^2}{2} + \frac{p^n}{\gamma - 1} \left(1 - \frac{\gamma u_{\text{R}}^n}{\Lambda_m} \right).\end{aligned}\tag{B.7}$$

Finally, let us return to the radial component of the velocity, described by the first line in Eqs. (B.5). This equation can be considered as a linear relation between $\delta u_{\text{R}} = u^{n+1} - u_{\text{R}}^n$ and $\delta p = p^{n+1} - p^n$: where:

$$\delta u_{\text{R}} = \frac{\Delta t_b}{\bar{\rho}} (S_{\rho u_{\text{R}}} - u_{\text{R}}^n S_{\rho}) + \frac{\delta p}{\bar{\rho} \Lambda_m}.\tag{B.8}$$

Eliminating δu_{R} from Eq. Eq. (B.5) with the use of Eq. (B.8) results in a quadratic equation,

$$\alpha (\delta p)^2 - \beta \delta p + \varepsilon = 0\tag{B.9}$$

that can be solved

$$\delta p = \frac{2\varepsilon}{\beta + \sqrt{\beta^2 - 4\alpha\varepsilon}},\tag{B.10}$$

where

$$\begin{aligned}\alpha &= \frac{(\gamma + 1)}{2(\gamma - 1)\bar{\rho}\Lambda_m^2}, & \beta &= \frac{1}{\gamma - 1} \left(1 - \frac{u_{\text{R}}^n}{\Lambda_m} - \frac{\Delta t_b (S_{\rho u_{\text{R}}} - u_{\text{R}}^n S_{\rho})}{\bar{\rho}\Lambda_m} - \frac{\gamma p^n}{\bar{\rho}\Lambda_m^2} \right), \\ \varepsilon &= \Delta t_b \left[S_{\varepsilon} + \frac{\mathbf{u}^2}{2} S_{\rho} - \mathbf{u}^n \cdot \mathbf{S}_{\rho \mathbf{u}} + \frac{\gamma p^n (S_{\rho u_{\text{R}}} - u_{\text{R}}^n S_{\rho})}{(\gamma - 1)\bar{\rho}\Lambda_m} \right] - \frac{(\Delta t_b)^2}{2\bar{\rho}} (\mathbf{S}_{\rho \mathbf{u}} - \mathbf{u}^n S_{\rho})^2.\end{aligned}\tag{B.11}$$

We note that formally $\delta p = 2\varepsilon/(\beta - \sqrt{\beta^2 - 4\alpha\varepsilon})$ is also a solution of Eq. (B.9). However, for small $\varepsilon \propto \Delta t_b$ it is not a physically meaningful solution as it does not tend to zero as $\Delta t_b \rightarrow 0$, while Eq. (B.10) automatically satisfies the correct asymptotic expansion, $\delta p = \varepsilon/\beta + O[\varepsilon^2]$.

With δp obtained from Eq. (B.10) one can find $p^{n+1} = p^n + \delta p$ and solve for δu_R from Eq. (B.8), then solve $u_R^{n+1} = u_R^n + \delta u_R$ and derive the density from Eq. (B.4): $\rho^{n+1} = \bar{\rho}/(1 - u_R^{n+1}/\Lambda_m)$. This way all primitive variables are recovered.

Appendix B.3. Numerical Hydrodynamics Test

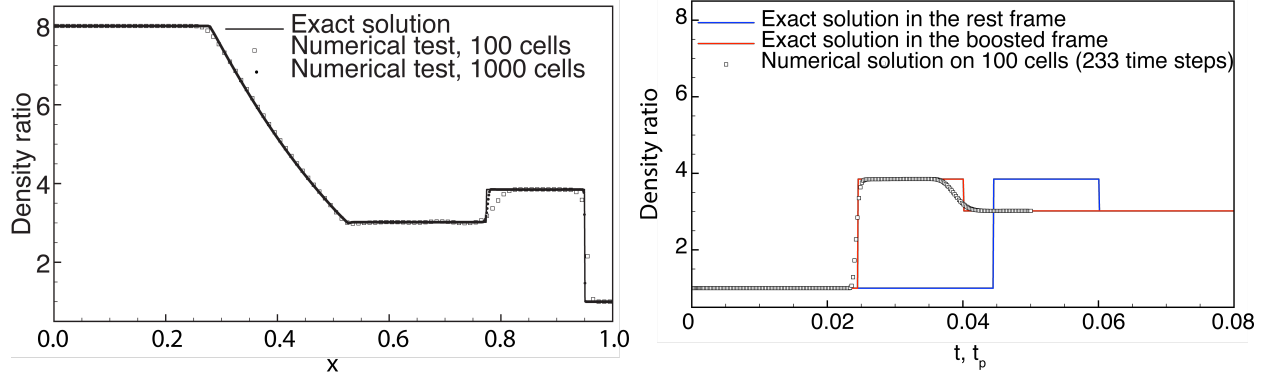


Figure B.6: Solution of the Riemann problem for a gas with $\gamma = 5/3$ with the initial condition: $\rho = 8$, $u = 0$ and $p = 480$ for $x < 0.5$; $\rho = 1$, $u = 0$ and $p = 1$ for $x > 0.5$. **Left panel:** Density ratio as a function of x in the boosted frame at time $t_b = 0.022$: the solid line shows the exact solution (also shown with the red line in Fig. 3); with symbols the numerical test solution is presented on 100 and 1000 cells. **Right panel:** Time profile of density at $x = 1$. Red line is the solution in the boosted frame, blue line is the solution in the rest frame. $\rho(t_b)$ predicts the solution in the rest frame, $\rho(t)$ with the time offset of 0.02 (both lines are the same as those in Fig. 3); symbols show the test simulation results at 233 time steps, with 100 cells per an interval, $(0, 1)$, of x .

To test the proposed scheme, we solved numerically the Riemann problem with discontinuous initial condition as described in Section 4 and illustrated in Fig. 3 and compare the obtained numerical results with the exact solutions provided there. The numerical fluxes are calculated based on the exact Riemann solver (the *Godunov scheme*) as described and coded by Toro (2009). To achieve second order of accuracy, a *limited interpolation procedure* is applied to get left and right interpolated states of primitive variables at each face of the control volumes to be used as the inputs for the numerical flux. The two-stage Runge-Kutta scheme is used for time integration.

In our numerical example the interval, $(0, 1)$ of the 1-D coordinate, x , is split into 100 equally spaced cells with a mesh size of 0.01 and an initial discontinuity is located at $x=0.5$. To the right from this location, the boosted frame is used in a way that the time offset at the right boundary reaches 0.02, corresponding to a limiting speed of $\Lambda_m = 0.5/0.02 = 25$. In Fig. B.6 the top panel shows the density distribution over x at time 0.022. The simulation took 105 time steps with a Courant-Friedrichs-Levi (CFL) number of 0.9. The agreement with the exact solution is reasonable with 100 cells and becomes nearly perfect with 1000 cells (1015 time steps). In the bottom panel the time evolution of density at $x = 1$ is presented. The blue line (rest frame) and red line (boosted frame) are identical to those provided in the right panel of Fig. 3) and show the exact solution. By symbols we present the numerical test result. Keeping the same spatial resolution of 0.01, i.e., using 100 cells over the interval of $(0, 1)$, we extend the computational

domain to $(-0.5, 1.5)$, to reduce the effect from the boundaries of the domain. For the interval of simulation time, $(0, 0.05)$, we show results after 233 time steps obtained in the boosted frame. The test demonstrates a reasonable quality of computational results and can serve as a proof of principle of the proposed forecast system: the numerical solution with time offset is possible.

Appendix C. Numerical Algorithm for Solving the Boosted MHD Equations

To solve Eq. (25) numerically, the vectors of magnetic field, velocity and their fluxes can be conveniently split into the radial velocity/field and the “horizontal” components, perpendicular to the radial direction:

$$B_R = \hat{\mathbf{e}}_R \cdot \mathbf{B}, \quad \mathbf{B}_\perp = \mathbf{B} - B_R \hat{\mathbf{e}}_R, \quad u_R = \hat{\mathbf{e}}_R \cdot \mathbf{u}, \quad \mathbf{u}_\perp = \mathbf{u} - u_R \hat{\mathbf{e}}_R, \quad \text{etc.} \quad (\text{C.1})$$

With these transformations the governing equations become:

$$\begin{aligned} \frac{\partial}{\partial t_b} \left[\rho \left(1 - \frac{u_R}{\Lambda_m} \right) \right] &= S_\rho \\ \frac{\partial}{\partial t_b} \left[\rho \left(1 - \frac{u_R}{\Lambda_m} \right) u_R - \frac{1}{\Lambda_m} \left(P + \frac{B_\perp^2}{2\mu_0} \right) \right] &= S_{\rho u_R} \\ \frac{\partial}{\partial t_b} \left[\rho \left(1 - \frac{u_R}{\Lambda_m} \right) \mathbf{u}_\perp \right] + \frac{B_R}{\Lambda_m \mu_0} \frac{\partial \mathbf{B}_\perp}{\partial t_b} &= \mathbf{S}_{\rho \mathbf{u}_\perp} \\ \left(1 - \frac{u_R}{\Lambda_m} \right) \frac{\partial B_R}{\partial t_b} &= S_{B_R} \\ \frac{\partial}{\partial t_b} \left[\left(1 - \frac{u_R}{\Lambda_m} \right) \mathbf{B}_\perp \right] + \frac{B_R}{\Lambda_m} \frac{\partial \mathbf{u}_\perp}{\partial t_b} &= \mathbf{S}_{\mathbf{B}_\perp} \end{aligned} \quad (\text{C.2})$$

The energy equation,

$$\begin{aligned} \frac{\partial}{\partial t_b} \left[\frac{\rho u^2 \left(1 - \frac{u_R}{\Lambda_m} \right)}{2} + \frac{P \left(1 - \frac{\gamma u_R}{\Lambda_m} \right)}{\gamma - 1} + \frac{B_\perp^2 \left(1 - \frac{2u_R}{\Lambda_m} \right) + B_R^2}{2\mu_0} \right] + \\ + \frac{B_R}{\Lambda_m \mu_0} \left[\frac{\partial (\mathbf{u}_\perp \cdot \mathbf{B}_\perp)}{\partial t_b} - u_R \frac{\partial B_R}{\partial t_b} \right] &= S_\varepsilon, \end{aligned}$$

can be obtained in a more convenient form by multiplying the radial field equation by B_R/μ_0 and subtracting the result from the energy equation:

$$\frac{\partial}{\partial t_b} \left[\frac{\rho u^2 \left(1 - \frac{u_R}{\Lambda_m} \right)}{2} + \frac{P \left(1 - \frac{\gamma u_R}{\Lambda_m} \right)}{\gamma - 1} + \frac{B_\perp^2 \left(1 - \frac{2u_R}{\Lambda_m} \right)}{2\mu_0} \right] + \frac{B_R}{\Lambda_m \mu_0} \frac{\partial (\mathbf{u}_\perp \cdot \mathbf{B}_\perp)}{\partial t_b} = S_\varepsilon - \frac{B_R}{\mu_0} S_{B_R}. \quad (\text{C.3})$$

Appendix C.1. Algorithm

Within the framework of finite volume numerical methods, the governing equations (Eqs. C.2) can be integrated over control volume using Gauss’ theorem, then the RHS of the equations are

calculated as the sum of *numerical fluxes* through the faces of the *control volume*, divided by the magnitude of control volume. Once the numerical solution is known at the time instant $t_b = t^n$, and the numerical fluxes and sources on the RHS of Eqs. (C.2) are all calculated, the solution at the next time level, $t_b = t^{n+1} = t^n + dt$ can be found by integrating the equations over time, giving:

$$\begin{aligned}
\tilde{U}_\rho^{n+1} &= \Delta t_b S_\rho + \tilde{U}_\rho^n, & \tilde{U}_\rho^n &= \rho^n \left(1 - \frac{u_R^n}{\Lambda_m} \right) \\
\tilde{U}_{\rho u_R}^{n+1} &= \Delta t_b S_{\rho u_R} + \tilde{U}_{\rho u_R}^n, & \tilde{U}_{\rho u_R}^n &= \rho^n \left(1 - \frac{u_R^n}{\Lambda_m} \right) u_R^n - \frac{1}{\Lambda_m} \left(p^n + \frac{(\mathbf{B}_\perp^n)^2}{2\mu_0} \right), \\
\tilde{U}_{\rho \mathbf{u}_\perp}^{n+1} &= \Delta t_b \mathbf{S}_{\rho \mathbf{u}_\perp} + \tilde{U}_{\rho \mathbf{u}_\perp}^n, & \tilde{U}_{\rho \mathbf{u}_\perp}^n &= \rho^n \left(1 - \frac{u_R^n}{\Lambda_m} \right) \mathbf{u}_\perp^n + \frac{\bar{B}_R}{\Lambda_m \mu_0} \mathbf{B}_\perp^n, \\
\left(1 - \frac{\bar{u}_R}{\Lambda_m} \right) B_R^{n+1} &= \Delta t_b S_{B_R} + \left(1 - \frac{\bar{u}_R}{\Lambda_m} \right) B_R^n \\
\tilde{U}_{\mathbf{B}_\perp}^{n+1} &= \Delta t_b \mathbf{S}_{\mathbf{B}_\perp} + \tilde{U}_{\mathbf{B}_\perp}^n, & \tilde{U}_{\mathbf{B}_\perp}^n &= \left(1 - \frac{u_R^n}{\Lambda_m} \right) \mathbf{B}_\perp^n + \frac{\bar{B}_R}{\Lambda_m} \mathbf{u}_\perp^n \\
\tilde{U}_\varepsilon^{n+1} &= \Delta t_b \left(S_\varepsilon - \frac{\bar{B}_R}{\mu_0} S_{B_R} \right) + \tilde{U}_\varepsilon^n, \\
\tilde{U}_\varepsilon^n &= \frac{\rho^n (\mathbf{u}^n)^2}{2} \left(1 - \frac{u_R^n}{\Lambda_m} \right) + \frac{p^n \left(1 - \frac{\gamma u_R^n}{\Lambda_m} \right)}{\gamma - 1} + \frac{(\mathbf{B}_\perp^n)^2 \left(1 - \frac{2u_R^n}{\Lambda_m} \right)}{2\mu_0} + \frac{\bar{B}_R}{\Lambda_m \mu_0} (\mathbf{u}_\perp^n \cdot \mathbf{B}_\perp^n).
\end{aligned} \tag{C.4}$$

The coefficient, \bar{u}_R , multiplied by the time derivative, $\partial B_R / \partial t_b$ in the field equations in Eqs. (C.2) is present in both B_R^n and B_R^{n+1} states in Eqs. (C.4). It originates from the explicit source term, $-u_R \nabla \cdot \mathbf{B}$, contributing to S_{B_R} , hence, it is known when Eqs. (C.4) needs to be solved. Therefore, B_R^{n+1} , can be solved explicitly. For another coefficient, \bar{B}_R , which also stands out of time derivatives and is present in both n th and $(n+1)$ th states, may be also solved explicitly as $\bar{B}_R = \frac{1}{2} (B_R^{n+1} + B_R^n)$:

$$B_R^{n+1} = B_R^n + \frac{\Delta t_b S_{B_R}}{1 - \frac{\bar{u}_R}{\Lambda_m}}, \quad \bar{B}_R = B_R^n + \frac{\Delta t_b S_{B_R}}{2 \left(1 - \frac{\bar{u}_R}{\Lambda_m} \right)}. \tag{C.5}$$

To simplify the algorithm, we follow the steps described in [Appendix B.2](#). First, we use Eq. (B.4) to eliminate the densities, ρ^n, ρ^{n+1} , from the expressions for $\tilde{U}_{\rho u_R}, \tilde{U}_{\rho \mathbf{u}_\perp}$ and \tilde{U}_ε . Now the equations for these conserved variables are:

$$\begin{aligned}
\tilde{U}_{\rho u_R}^{n+1} &= \Delta t_b (S_{\rho u_R} - u_R^n S_\rho) + \tilde{U}_{\rho u_R}^n, & \tilde{U}_{\rho u_R}^n &= \bar{\rho} u_R^n - \frac{1}{\Lambda_m} \left(p^n + \frac{(\mathbf{B}_\perp^n)^2}{2\mu_0} \right), \\
\tilde{U}_{\rho \mathbf{u}_\perp}^{n+1} &= \Delta t_b (\mathbf{S}_{\rho \mathbf{u}_\perp} - \mathbf{u}_\perp^n S_\rho) + \tilde{U}_{\rho \mathbf{u}_\perp}^n, & \tilde{U}_{\rho \mathbf{u}_\perp}^n &= \bar{\rho} \mathbf{u}_\perp^n + \frac{\bar{B}_R}{\Lambda_m \mu_0} \mathbf{B}_\perp^n, \\
\tilde{U}_\varepsilon^{n+1} &= \Delta t_b \left(S_\varepsilon - \frac{(\mathbf{u}^n)^2}{2} S_\rho - \frac{\bar{B}_R}{\mu_0} S_{B_R} \right) + \tilde{U}_\varepsilon^n, \\
\tilde{U}_\varepsilon^n &= \frac{\bar{\rho} (\mathbf{u}^n)^2}{2} + \frac{p^n \left(1 - \frac{\gamma u_R^n}{\Lambda_m} \right)}{\gamma - 1} + \frac{(\mathbf{B}_\perp^n)^2 \left(1 - \frac{2u_R^n}{\Lambda_m} \right)}{2\mu_0} + \frac{\bar{B}_R}{\Lambda_m \mu_0} (\mathbf{u}_\perp^n \cdot \mathbf{B}_\perp^n).
\end{aligned} \tag{C.6}$$

Next, we express \mathbf{u}_\perp^{n+1} in terms of the yet unknown \mathbf{B}_\perp^{n+1} :

$$\mathbf{u}_\perp^{n+1} = \frac{\Delta t_b}{\bar{\rho}} (\mathbf{S}_{\rho\mathbf{u}_\perp} - \mathbf{u}_\perp^n S_\rho) + \mathbf{u}_\perp^n - \frac{\bar{B}_R}{\Lambda_m \mu_0 \bar{\rho}} (\mathbf{B}_\perp^{n+1} - \mathbf{B}_\perp^n) \quad (\text{C.7})$$

and then use Eq. (C.7) to eliminate \mathbf{u}_\perp^{n+1} from the equations for the energy and the magnetic field.

Finally, we obtain the finite volume scheme for the reduced conserved variables:

$$\begin{aligned} \tilde{U}_{\rho u_R}^{n+1} &= \Delta t_b (S_{\rho u_R} - u_R^n S_\rho) + \tilde{U}_{\rho u_R}^n, \quad \tilde{U}_{\rho u_R}^n = \bar{\rho} u_R^n - \frac{1}{\Lambda_m} \left(p^n + \frac{(\mathbf{B}_\perp^n)^2}{2\mu_0} \right), \\ \tilde{\mathbf{U}}_{\mathbf{B}_\perp}^{n+1} &= \Delta t_b \left[\mathbf{S}_{\mathbf{B}_\perp} - \frac{\bar{B}_R}{\bar{\rho} \Lambda_m} (\mathbf{S}_{\rho\mathbf{u}_\perp} - \mathbf{u}_\perp^n S_\rho) \right] + \tilde{\mathbf{U}}_{\mathbf{B}_\perp}^n, \quad \tilde{\mathbf{U}}_{\mathbf{B}_\perp}^n = \left(1 - \frac{u_R^n}{\Lambda_m} - \frac{\bar{V}_{AR}^2}{\Lambda_m^2} \right) \mathbf{B}_\perp^n, \\ \tilde{U}_\varepsilon^{n+1} &= \Delta t_b \left[S_\varepsilon - \frac{(\mathbf{u}^n)^2}{2} S_\rho - \left(\mathbf{u}_\perp^n + \frac{\bar{B}_R \mathbf{B}_\perp^n}{\mu_0 \Lambda_m \bar{\rho}} \right) \cdot (\mathbf{S}_{\rho\mathbf{u}_\perp} - \mathbf{u}_\perp^n S_\rho) - \frac{\bar{B}_R}{\mu_0} S_{B_R} \right] - \\ &\quad - \frac{(\Delta t_b)^2 (\mathbf{S}_{\rho\mathbf{u}_\perp} - \mathbf{u}_\perp^n S_\rho)^2}{2\bar{\rho}} + \tilde{U}_\varepsilon^n, \\ \tilde{U}_\varepsilon^n &= \frac{\bar{\rho} (u_R^n)^2}{2} + \left(1 - \frac{\gamma u_R^n}{\Lambda_m} \right) \frac{p^n}{\gamma - 1} + \left(1 - \frac{2u_R^n}{\Lambda_m} - \frac{\bar{V}_{AR}^2}{\Lambda_m^2} \right) \frac{(\mathbf{B}_\perp^n)^2}{2\mu_0}, \end{aligned} \quad (\text{C.8})$$

where $\bar{V}_{AR}^2 = \bar{B}_R^2 / (\mu_0 \bar{\rho})$ is the square of the Alfvén wave speed in the radial direction.

Appendix C.2. Solving for Primitive Variables

Eqs. (C.8) can be solved and the unknown $\mathcal{P} = (u_R^{n+1}, \mathbf{B}_\perp^{n+1}, p^{n+1})$ can be found using the method described in Appendix A.2. The conserved variables, $\tilde{U}^{(n+1,h)}$, at iteration h can be expressed in terms of the primitive variables, $\mathcal{P}^{(n+1,h)} = (u_R^{(n+1,h)}, \mathbf{B}_\perp^{(n+1,h)}, p^{(n+1,h)})$:

$$\begin{aligned} \tilde{U}_{\rho u_R}^{(n+1,h)} &= \bar{\rho} u_R^{(n+1,h)} - \frac{1}{\Lambda_m} \left[p^{(n+1,h)} + \frac{(\mathbf{B}_\perp^{(n+1,h)})^2}{2\mu_0} \right], \\ \tilde{\mathbf{U}}_{\mathbf{B}_\perp}^{(n+1,h)} &= \left(1 - \frac{u_R^{(n+1,h)}}{\Lambda_m} - \frac{\bar{V}_{AR}^2}{\Lambda_m^2} \right) \mathbf{B}_\perp^{(n+1,h)}, \\ \tilde{U}_\varepsilon^{(n+1,h)} &= \frac{\bar{\rho} (u_R^{(n+1,h)})^2}{2} + \left(1 - \frac{\gamma u_R^{(n+1,h)}}{\Lambda_m} \right) \frac{p^{(n+1,h)}}{\gamma - 1} + \left(1 - \frac{2u_R^{(n+1,h)}}{\Lambda_m} - \frac{\bar{V}_{AR}^2}{\Lambda_m^2} \right) \frac{(\mathbf{B}_\perp^{(n+1,h)})^2}{2\mu_0}. \end{aligned} \quad (\text{C.9})$$

At time level $n + 1$ we start the iteration process ($h = 0$) from quantities obtained at the previous time level, t^n : $\mathcal{P}^{(n+1,0)} = \mathcal{P}^n$. We use Eqs. (A.9) to solve the increments of the primitive variables, $\delta^{h+1} \mathcal{P} = \mathcal{P}^{(n+1,h+1)} - \mathcal{P}^{(n+1,h)}$. We linearize the increments of the conserved variables using

Eq. (A.11):

$$\begin{aligned}
\tilde{U}_{\rho u_R}^{(n+1,h+1)} - \tilde{U}_{\rho u_R}^{(n+1,h)} &\approx \bar{\rho} \delta^{h+1} u_R - \frac{\mathbf{B}_\perp^{(n+1,h)}}{\mu_0 \Lambda_m} \cdot \delta^{h+1} \mathbf{B}_\perp - \frac{1}{\Lambda_m} \delta^{h+1} p, \\
\tilde{U}_{\mathbf{B}_\perp}^{(n+1,h+1)} - \tilde{U}_{\mathbf{B}_\perp}^{(n+1,h)} &\approx -\frac{\mathbf{B}_\perp^{(n+1,h)}}{\Lambda_m} \delta^{h+1} u_R + \left(1 - \frac{u_R^{(n+1,h)}}{\Lambda_m} - \frac{\bar{V}_{A_R}^2}{\Lambda_m^2}\right) \delta^{h+1} \mathbf{B}_\perp, \\
\tilde{U}_\xi^{(n+1,h+1)} - \tilde{U}_\xi^{(n+1,h)} - u_R^{(n+1,h)} \left(\tilde{U}_{\rho u_R}^{(n+1,h+1)} - \tilde{U}_{\rho u_R}^{(n+1,h)}\right) - \\
&- \frac{\mathbf{B}_\perp^{(n+1,h)}}{\mu_0} \cdot \left(\tilde{U}_{\mathbf{B}_\perp}^{(n+1,h+1)} - \tilde{U}_{\mathbf{B}_\perp}^{(n+1,h)}\right) \approx -\frac{\gamma p^{(n+1,h)}}{(\gamma-1)\Lambda_m} \delta^{h+1} u_R + \frac{1 - u_R^{(n+1,h)}/\Lambda_m}{\gamma-1} \delta^{h+1} p,
\end{aligned} \tag{C.10}$$

Here we introduced the increment of the (non-conserved) *internal energy* in the last equation instead of the increment in the full energy. This helps us to simplify the last (and quite cumbersome) equation in Eqs. (A.9) by subtracting a reasonably chosen linear combination of the other equations. The iterated energy defects in the RHS of Eqs. (A.9) can be derived from Eqs. (A.10 and C.9):

$$\begin{aligned}
\Delta_{\rho u_R}^h &= \begin{cases} \Delta t_b (S_{\rho u_R} - u_R^n S_\rho), & h = 0 \\ \Delta_{\rho u_R}^{h-1} + \tilde{U}_{\rho u_R}^{(n+1,h-1)} - \tilde{U}_{\rho u_R}^{(n+1,h)}, & h \geq 1 \end{cases} \\
\Delta_{\mathbf{B}_\perp}^h &= \begin{cases} \Delta t_b \left[\mathbf{S}_{\mathbf{B}_\perp} - \frac{\bar{B}_R}{\rho \Lambda_m} (\mathbf{S}_{\rho \mathbf{u}_\perp} - \mathbf{u}_\perp^n S_\rho) \right], & h = 0 \\ \Delta_{\mathbf{B}_\perp}^{h-1} + \tilde{U}_{\mathbf{B}_\perp}^{(n+1,h-1)} - \tilde{U}_{\mathbf{B}_\perp}^{(n+1,h)}, & h \geq 1 \end{cases} \\
\Delta_\xi^h &= \begin{cases} \Delta t_b \left[S_\xi + \frac{(\mathbf{u}^n)^2}{2} S_\rho - \mathbf{u}^n \cdot \mathbf{S}_{\rho \mathbf{u}} - \frac{\bar{B}_R}{\mu_0} S_{B_R} - \frac{\mathbf{B}_\perp^n}{\mu_0} \cdot \mathbf{S}_{\mathbf{B}_\perp} \right] \\ \quad - \frac{(\Delta t_b)^2 (\mathbf{S}_{\rho \mathbf{u}_\perp} - \mathbf{u}_\perp^n S_\rho)^2}{2\bar{\rho}}, & h = 0 \\ \Delta_\xi^{h-1} + u_R^{(n+1,h-1)} \Delta_{\rho u_R}^{h-1} + \frac{\mathbf{B}_\perp^{(n+1,h-1)}}{\mu_0} \cdot \Delta_{\mathbf{B}_\perp}^{h-1} \\ \quad + \left[\tilde{U}_\xi^{(n+1,h-1)} - \tilde{U}_\xi^{(n+1,h)} \right] - u_R^{(n+1,h)} \Delta_{\rho u_R}^h - \frac{\mathbf{B}_\perp^{(n+1,h)}}{\mu_0} \cdot \Delta_{\mathbf{B}_\perp}^h, & h \geq 1 \end{cases}
\end{aligned} \tag{C.11}$$

Note that in the energy equation we moved into the second line the higher order terms. Solving the system of three linear equations, Eq. (A.9) with the LHS derived from Eqs. (A.11 and C.10)

$$\begin{pmatrix} \bar{\rho} & -\frac{\mathbf{B}_\perp^{(n+1,h)}}{\mu_0 \Lambda_m} & -\frac{1}{\Lambda_m} \\ -\frac{\mathbf{B}_\perp^{(n+1,h)}}{\Lambda_m} & \left(1 - \frac{u_R^{(n+1,h)}}{\Lambda_m} - \frac{\bar{V}_{A_R}^2}{\Lambda_m^2}\right) \mathbf{I} & 0 \\ -\frac{\gamma p^{(n+1,h)}}{(\gamma-1)\Lambda_m} & 0 & \frac{1 - u_R^{(n+1,h)}/\Lambda_m}{\gamma-1} \end{pmatrix} \cdot \begin{pmatrix} \delta^{h+1} u_R \\ \delta^{h+1} \mathbf{B}_\perp \\ \delta^{h+1} p \end{pmatrix} = \begin{pmatrix} \Delta_{\rho u_R}^h \\ \Delta_{\mathbf{B}_\perp}^h \\ \Delta_\xi^h \end{pmatrix} \tag{C.12}$$

is straightforward and can be generalized for many extensions of the MHD model. All increments in the primitive variables are expressed in terms of $\delta^{h+1}u_R$:

$$\begin{pmatrix} \delta^{h+1}\mathbf{B}_\perp \\ \delta^{h+1}p \end{pmatrix} = \mathbf{D}^{-1} \cdot \left[\begin{pmatrix} \Delta_{\mathbf{B}_\perp}^h \\ \Delta_\xi^h \end{pmatrix} - \mathbf{A}_{\mathcal{P},u_R} \delta^{h+1}u_R \right] \quad (\text{C.13})$$

where

$$\mathbf{D} = \text{diag} \left[\left(1 - \frac{u_R^{(n+1,h)}}{\Lambda_m} - \frac{\bar{V}_{AR}^2}{\Lambda_m^2} \right) \mathbf{I}, \frac{1 - u_R^{(n+1,h)}/\Lambda_m}{\gamma - 1} \right] \quad (\text{C.14})$$

is an easy-to-invert 4*4 diagonal matrix, \mathbf{D}^{-1} is its inverse, and

$$\mathbf{A}_{\mathcal{P},u_R} = \left(-\frac{\mathbf{B}_\perp^{(n+1,h)}}{\Lambda_m}, -\frac{\gamma p^{(n+1,h)}}{(\gamma - 1) \Lambda_m} \right)^T \quad (\text{C.15})$$

is a vector of the derivatives of the conserved variables with respect of u_R . The solution for $\delta^{h+1}u_R$ is then given by the first of Eqs. (C.12):

$$\delta^{h+1}u_R = \frac{\Delta_{\rho u_R}^h - \mathbf{A}_{u_R,\mathcal{P}} \cdot \mathbf{D}^{-1} \cdot \begin{pmatrix} \Delta_{\mathbf{B}_\perp}^h \\ \Delta_\xi^h \end{pmatrix}}{\bar{\rho} - \mathbf{A}_{u_R,\mathcal{P}} \cdot \mathbf{D}^{-1} \cdot \mathbf{A}_{\mathcal{P},u_R}}. \quad (\text{C.16})$$

Here

$$\mathbf{A}_{u_R,\mathcal{P}} = \left(-\frac{\mathbf{B}_\perp^{(n+1,h)}}{\mu_0 \Lambda_m}, -\frac{1}{\Lambda_m} \right)^T \quad (\text{C.17})$$

is a vector of the derivatives of the radial stress over the primitive variables multiplied by a factor of $-1/\Lambda_m$. After some algebra one can prove that if in all iterated states, $\mathcal{P}^{(n+1,h)}$, the fast magnetosonic speed in the radial direction does not exceed Λ_m , both matrix \mathbf{D} is positive definite (hence, non-singular) and denominator in Eq. (C.16) is positive, thus ensuring the convergence of the iteration procedure.

For systems that are more complex than MHD with a single scalar pressure (such more complex systems can also include electron pressure, Alfvén wave turbulence, etc), the basic structure of Eq. (C.16) that gives the solution for $\delta^{h+1}u_R$ remains the same and only the length of vectors in Eqs. (C.15 and C.17) increases.

With known $\delta^{h+1}u_R$, the other increments of primitive variables can be solved from Eqs. (C.13) and then a new iteration for primitive variables can be found, $\mathcal{P}^{(n+1,h+1)} = \mathcal{P}^{(n+1,h)} + \delta^{h+1}\mathcal{P}$. If the desired accuracy has not been achieved, the RHS in Eqs. (C.12) can be iterated using Eqs. (C.11); otherwise, the (h+1)st iteration is assigned to the time level, t^{n+1} : $\mathcal{P}^{(n+1,h+1)} \rightarrow \mathcal{P}^{n+1}$ for radial velocity, perpendicular magnetic field and pressure. The radial magnetic field should be obtained from Eq. (C.5). Once \mathbf{B}_\perp^{n+1} is known, the perpendicular velocity can be found from Eq. (C.7). Finally, the density is solved from Eq. (B.4): $\rho^{n+1} = \bar{\rho} / (1 - u_R^{n+1}/\Lambda_m)$. This way all primitive variables are recovered.

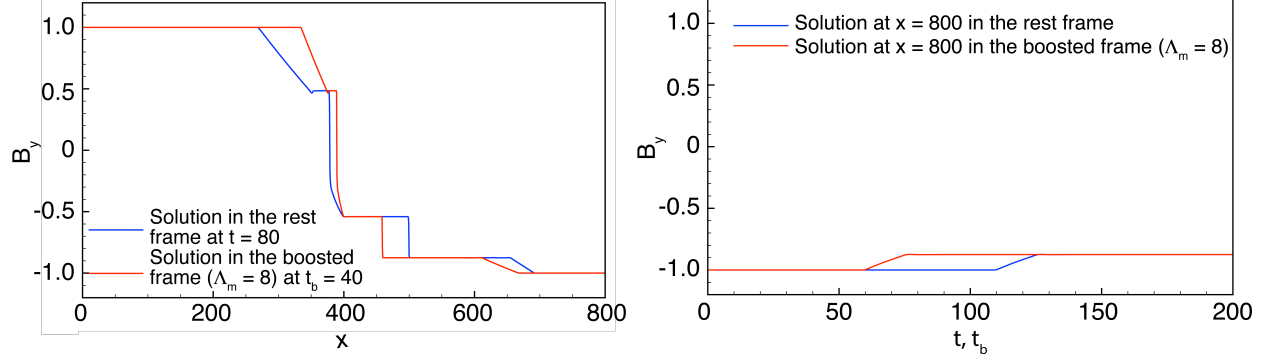


Figure C.7: Reference solution of the Riemann problem with the initial condition: $\mathcal{P} = (\rho, \mathbf{u}, \mathbf{B}, p) = (1, 0, 0, 0, \frac{3}{4}, 1, 0, 1)$ at $x < 400$; $\mathcal{P} = (\frac{1}{8}, 0, 0, 0, \frac{3}{4}, -1, 0, \frac{1}{10})$ at $x > 400$, for a gas with $\gamma = 7/5$. **Left panel:** Blue line shows the solution of MHD equations in the rest frame at the time, $t = 80$; red line presents the solution in the boosted frame at time $t_b = 40$. **Right panel:** Time profile of density at $x = 800$. Red line is the solution in the boosted frame, blue line is the solution in the rest frame. $B_y(t_b)$ predicts the solution in the rest frame, $B_y(t)$ with time offset of 50.

Appendix C.3. Numerical Example

As the test problem we solved numerically the [Brio and Wu \(1988\)](#) test case (we use the version published by [Cargo and Gallice, 1997](#)), on 800 cells at spatial resolution of $\Delta x = 1$. The initial discontinuity located at $x = 400$ separates states $\mathcal{P} = (\rho, \mathbf{u}, \mathbf{B}, p) = (1, 0, 0, 0, \frac{3}{4}, 1, 0, 1)$ at $x < 400$ and $\mathcal{P} = (\frac{1}{8}, 0, 0, 0, \frac{3}{4}, -1, 0, \frac{1}{10})$ at $x > 400$. As an “exact” solution, we solve the same problem on 4,000 cell with the resolution of $dx = 0.2$. The solution in the rest frame at time $t = 80$ as a function of $0 \leq x \leq 800$ is presented in the left panel of Fig. C.7 by the blue line.

Following Sec. 4.1, we can apply this result as an approximate solution of the Riemann problem in the rest frame, $\mathcal{P}_{\text{RS}}(\frac{x-400}{t})$, in the argument range of $-5 \leq \frac{x-400}{80} \leq 5$. In the right panel of Fig. C.7 the blue line shows this solution, $\mathcal{P}_{\text{RS}}(\frac{x-400}{t})$, at a fixed location, $x = 800$, as a function of time.

The solution of the Riemann problem in the rest frame can also be applied to get an “exact” solution in the boosted frame (similarly to Eq. 19):

$$\mathcal{P} = \begin{cases} \mathcal{P}_{\text{RS}}\left(\frac{x-400}{t_b}\right) & \text{if } 0 \leq x \leq 400 \\ \mathcal{P}_{\text{RS}}\left(\frac{\frac{x-400}{t_b}}{1 + \frac{1}{\Lambda_m} \frac{x-400}{t_b}}\right) & \text{if } 400 \leq x \leq 800. \end{cases} \quad (\text{C.18})$$

The reference solution obtained this way in the boosted frame is shown with red lines in Fig. C.7 with the choice of $\Lambda_m = 8$, corresponding to a time offset, $\Delta t_0 = 50$, at the right boundary. In the left panel we show the solution for the magnetic field as a function of x at time $t_b = 40$. Although the time interval in the boosted frame is twice shorter than the one used to get the rest frame solution, the distance traveled by the magnetic field perturbation propagating to the right is close in both cases as a result of the time offset. In the right panel the red line demonstrates the time evolution of the magnetic perturbation at $x = 800$. Comparison with the blue line clearly demonstrates the time offset, $\Delta t_0 = 50$, i.e., in the boosted frame the magnetic perturbation arrives to the right boundary much earlier.

Once the reference solution in the boosted frame is obtained, we can compare it with the numerical simulation results in the boosted frame. In all simulations we apply the iterative procedure to recover the primitive variables as described in [Appendix C.2](#) with the iteration convergence criterion as follows:

$$\|\delta^{h+1}u_R\| \leq 10^{-6}\Lambda_m. \quad (\text{C.19})$$

As a cross-check, we also simulated the numerical hydrodynamics test described in [Appendix B.3](#) applying the iterative procedure for the MHD equations to solve the problem where the magnetic field vanishes identically. The results do not show any noticeable difference from those obtained with the iteration-free procedure to solve for the primitive hydrodynamic variables described in [Appendix B.2](#).

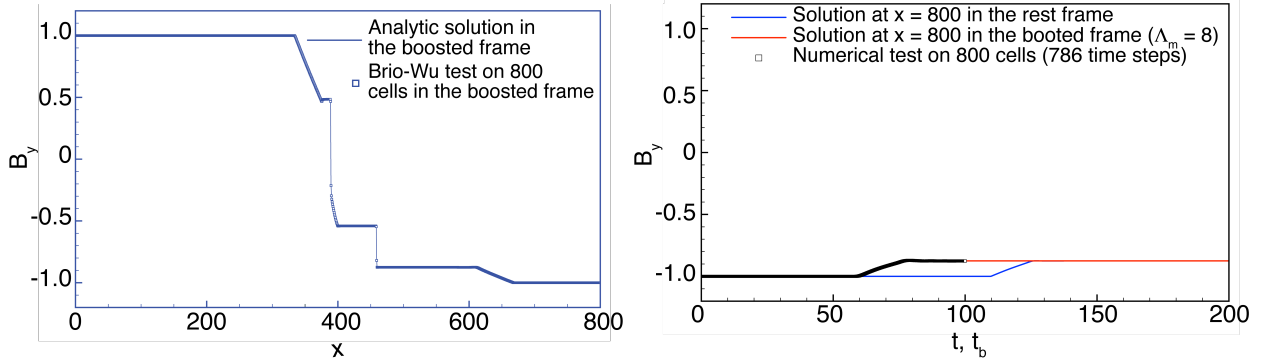


Figure C.8: Numerical solution of the [Brio and Wu \(1988\)](#) Riemann problem with the initial condition: $\mathcal{P} = (\rho, \mathbf{u}, \mathbf{B}, p) = (1, 0, 0, 0, \frac{3}{4}, 1, 0, 1)$ at $x < 400$; $\mathcal{P} = (\frac{1}{8}, 0, 0, 0, \frac{3}{4}, -1, 0, \frac{1}{10})$ at $x > 400$, for a gas with $\gamma = 7/5$, in the boosted frame with $\Lambda_m = 8$. **The Left panel:** magnetic field as a function of x at time $t_b = 40$: the solid line shows the exact solution (also shown with the red line in [Fig. C.7](#)); while symbols represent the numerical test solution on 800 cells. **Right panel:** Time profile of the magnetic field at $x = 800$. Red line is the exact solution in the boosted frame, blue line is the exact solution in the rest frame (both lines are the same as those in [Fig. C.7](#)); symbols show the numerical test result for an interval, $(0, 100)$ of t_b (at 786 time steps), with 800 cells per an interval, $(0, 800)$, of x .

As a full MHD test, we solved numerically the [Brio and Wu \(1988\)](#) problem in the boosted frame with $\Lambda_m = 8$ on 800 cells. We applied the *artificial wind* ([Sokolov et al., 2002](#)) numerical flux combined with limited reconstruction procedure to interpolate primitive variables to the faces. A two-stage Runge-Kutta scheme allowed us to achieve second order of accuracy in time. In the left panel of [Fig. C.8](#) we show the numerical result for the magnetic field distribution over x at time $t_b = 40$. The agreement with the reference solution in the boosted frame (which shown in the left panel of [Fig. C.7](#)) is remarkable.

To get the test result for time evolution at a fixed location, $x = 800$, we extend the computational domain by 400 cells at both sides, to reduce the effect of the computational domain boundaries on the numerical solution. The numerical result for the magnetic field at $x = 800$ as a function of time is shown in the right panel of [Fig. C.8](#) by symbols. For comparison, blue line and red line show the exact solution in the rest frame and in the boosted frame correspondingly (both lines are the same as those in [Fig. C.7](#)). The numerical result in the boosted frame both agrees with the exact solution in the boosted frame and perfectly “predicts” the solution in the rest frame with the time offset of $(800 - 400)/\Lambda_m = 50$.

Appendix D. Future Work on Numerical Algorithms

In the Appendices of this paper we discussed the major issues to be solved in applying our proposed approach to a simplified model of the solar wind. However, the choice of a more sophisticated model will require more analytic work. Specifically, the “non-conservative” model, in which instead of the full energy conservation law the non-conservative internal energy equation is used, which in the rest frame reads::

$$\frac{\partial}{\partial t} \frac{p}{\gamma - 1} + \nabla \cdot \left(\frac{p \mathbf{u}}{\gamma - 1} \right) + p \nabla \cdot \mathbf{u} = 0. \quad (\text{D.1})$$

In this equation the transformation of the velocity divergence should be applied in the boosted frame similarly to how the magnetic field divergence is treated in Sec. 5 and Appendix C: $\nabla \cdot \mathbf{u} \rightarrow \nabla \cdot \mathbf{u} - \frac{1}{\Lambda_m} \frac{\partial u_R}{\partial t_b}$. If the electron temperature is not assumed to be equal to the ion one this kind of equation also needs to be solved for the electron pressure. In this case electron internal energy and pressure contribute to the total energy and pressure, respectively, while the electron pressure needs to be solved from the following equation:

$$\frac{\partial}{\partial t} \frac{p_e}{\gamma_e - 1} + \nabla \cdot \left(\frac{p_e \mathbf{u}}{\gamma_e - 1} \right) + p_e \nabla \cdot \mathbf{u} = 0. \quad (\text{D.2})$$